RSC Advances

PAPER

View Article Online
View Journal | View Issue

Cite this: *RSC Adv.*, 2026, **16**, 30687

Efficient removal of mercury(II) ions using glutamic acid modified metal–organic frameworks: adsorption models, thermodynamics, and parameter optimization

Ahlem Guesmi,[a] Faisal K. Algethami,[a] Naoufel Ben Hamadi,[a] Wesam Abd El-Fattah,[a] Mohamed G. El-Desouky[b] and Ashraf A. El-Bindary*[cd]

The targeted removal of mercury(II) ions from contaminated aqueous systems presents a significant environmental issue, attributed to mercury's high toxicity, persistence in nature, and potential for bioaccumulation. This research focuses on the synthesis and assessment of a glutamic acid-functionalized silver metal–organic framework (NH_2-Ag-MOF) as an effective sorbent for the elimination of Hg(II) ions from water. The modified framework demonstrated remarkable properties, including a substantial surface area of 1750.49 $m^2\ g^{-1}$, a mesoporous structure with an average pore diameter of 3.84 nm, and a plethora of nitrogen-rich functional groups that markedly improved its affinity for mercury. Characterization techniques such as XRD, FT-IR, SEM, EDX, BET analysis, and XPS verified the successful functionalization of amine groups while preserving the structural integrity of the parent Ag-MOF. Batch adsorption experiments revealed that the uptake of Hg(II) was significantly affected by parameters including pH, dosage, temperature, and initial concentration, with a maximum adsorption capacity of 638.2 mg g^{-1} attained. The adsorption behavior was consistent with the Langmuir isotherm model and followed pseudo-second-order kinetics, indicative of monolayer chemisorption, supported by an adsorption energy value of 31.6 kJ mol^{-1}. Thermodynamic analysis showed a positive enthalpy change ($\Delta H° = 84.9$ kJ mol^{-1}) and negative changes in Gibbs free energy ($\Delta G°$), confirming that the adsorption process is endothermic and proceeds spontaneously. Furthermore, Density Functional Theory (DFT) calculations indicated that the binding of Hg(II) is facilitated through C=O coordination and electrostatic interactions with $-COO^-$ groups present. The adsorbent exhibited efficiency across five regeneration cycles.

Received 28th March 2026
Accepted 29th May 2026

DOI: 10.1039/d6ra02574a

rsc.li/rsc-advances

1. Introduction

The removal of mercury from wastewater is necessary for environmental protection and public health because of its high toxicity, persistence, and bioaccumulation potential. Mercury, when released into water bodies, can convert to methylmercury – a more toxic form that readily enters the food chain – accumulating in fish and eventually humans. Even trace amounts can be extremely hazardous as they affect the central nervous system, kidneys, and cardiovascular tissues with symptoms including neurological damage, cognitive deficits in adults and children, developmental issues in children, and reproductive problems. Unlike organic pollutants, which degrade naturally over time, mercury remains a persistent threat to aquatic environments. It disrupts microbial function and growth in aquatic plants while threatening fish and wildlife viability. Economically speaking as well; mercury pollution will raise the cost of water treatment reduce fisheries productivity and impose stringent regulations on industries. In this regard World Health Organization (WHO) and Environmental Protection Agency (EPA) have laid down discharge regulations that necessitate industries to come up with effective treatment solutions. Therefore making selective, efficient as well as reusable adsorbents for mercury removal very necessary in protecting human health and ecosystem plus compliance with regulations.[1]

The removal of mercury from wastewater has been addressed through a range of treatment technologies, each presenting distinct levels of efficacy and inherent drawbacks.[2–4] Conventional methodologies, such as chemical precipitation, facilitate the conversion of mercury ions into insoluble complexes of sulfide or hydroxide, enabling their extraction from the liquid

[a]*Chemistry Department, College of Science, Imam Mohammad Ibn Saud Islamic University (IMSIU), Riyadh 11623, Saudi Arabia*
[b]*Egyptian Propylene and Polypropylene Company, Port Said 42511, Egypt*
[c]*Health Sciences Research Center (HSRC), Deanship of Scientific Research, Imam Mohammad Ibn Saud Islamic University (IMSIU), Riyadh 13317, Saudi Arabia*
[d]*Chemistry Department, Faculty of Science, Damietta University, Damietta 34517, Egypt. E-mail: abindary@du.edu.eg*

phase; however, this approach often generates substantial quantities of toxic sludge necessitating expensive post-treatment processes.[5] Ion-exchange methods employ synthetic resins that can replace mercury ions with more benign ions such as hydrogen or sodium, yet their selectivity and operational efficiency are frequently undermined by the presence of competing cations typically found in industrial wastewater.[6] Membrane-based technologies, including reverse osmosis, nanofiltration, and ultrafiltration, achieve substantial mercury removal through the physical separation of ions by semi-permeable membranes; however, these technologies suffer from issues related to membrane fouling, stringent operational pressure requirements, and elevated maintenance expenses. Electrochemical methodologies, encompassing electro-coagulation and electrodeposition, facilitate mercury removal by destabilizing ionic species or depositing them on electrodes, yet their complexity and high energy requirements constrain their large-scale applicability.[7,8]

Metal–Organic Frameworks (MOFs) are advanced adsorbent materials recognized for removing heavy metals from wastewater due to their outstanding physicochemical properties and structural versatility. Unlike traditional sorbents such as activated carbon and zeolites, MOFs have extremely high surface areas, often exceeding thousands of $m^2\ g^{-1}$, providing numerous active sites for binding metal ions and enhancing adsorption capacity.[9,10] Their customizable porous structure allows for precise control of pore sizes and functional traits, enabling the selective capture of metals like Hg(II), Pb(II), Cd(II), and Cr(VI) in complex aqueous environments. MOFs can be functionalized with various donor groups, including $-NH_2$ and –COOH, enhancing metal coordination through chelation and electrostatic attraction.[11] This results in improved selectivity and stronger binding compared to conventional adsorbents. Another advantage of MOFs is their strong chemical and thermal stability, making them durable against harsh wastewater conditions, including variable pH and high ionic strength. Additionally, their three-dimensional channels facilitate rapid adsorption, promoting swift metal ion diffusion into the framework.[12] Many MOFs can be regenerated multiple times with little performance loss, reducing operational costs and secondary waste. The ability to tailor their structure at the molecular level enables researchers to create MOFs for specific pollutants, promoting application-specific adsorption systems. These features make MOFs optimal for effective and sustainable wastewater treatment involving heavy metals.[13]

The introduction of glutamic acid into silver-based metal–organic frameworks (Ag-MOFs) substantially enhances their efficiency in extracting Hg(II) ions from wastewater, primarily due to the introduction of multifunctional active sites and optimized surface chemistry.[14] Glutamic acid has amino ($-NH_2$) and carboxyl (–COOH) groups that are strong electron-donating ligands capable of forming stable chelates with mercury ions. The grafting of these functional groups onto Ag-MOF increases the binding site density, which increases affinity, selectivity, and adsorption capacity for Hg(II) ions.[15] The amine group assists coordination and interaction with positively charged mercury while the carboxyl group provides an additional complexation pathway; this results in synergistic adsorption mechanisms that are more effective than unmodified Ag-MOF.[16] Furthermore, glutamic acid increases hydrophilicity and water dispersion to enhance diffusion kinetics as well as interaction strength between Hg(II) ions and the framework. It stabilizes the Ag-MOF structure by hydrogen bonding and strengthening metal–ligand interactions which increases resistance to structural degradation under varying pH and ionic conditions.[17] This functionalization not only increases the overall adsorption capacity but also increases selectivity such that the modified NH_2-Ag-MOF can preferentially capture Hg(II) ions in the presence of competing metal ions found in industrial wastewater.[18,19] Additionally, improved regeneration efficiency is observed since strong but reversible bonds allow for effective desorption and reuse over several cycles without performance decline. All these advantages together emphasize how strategically important glutamic acid modification is to convert Ag-MOF into a highly selective, stable, and recyclable adsorbent that can efficiently remediate mercury from contaminated water sources.[20]

The Box–Behnken Design (BBD) significantly enhances the optimization of adsorption processes compared to the traditional one-factor-at-a-time approach due to its systematic integration of multiple factors. As a key component of Response Surface Methodology (RSM), BBD facilitates an efficient exploration of various parameters such as pH, adsorbent dosage, contact time, and initial metal concentration while minimizing the number of required experiments.[21] This not only alleviates laboratory workload but also reduces costs, time, and reagent consumption, resulting in statistically robust models for optimization. Unlike conventional methods that assess factors individually, BBD provides a platform to understand how these variables interact collaboratively to maximize adsorption performance and determine ideal conditions.[22] By avoiding extreme values in experimental design that may lead to unreliable outcomes, the approach further enhances safety and consistency. Moreover, BBD yields predictive mathematical models along with response surface plots that allow for predicting adsorption behavior across different scenarios without additional experiments, an essential characteristic when translating laboratory results into industrial applications.[23] Combining statistical rigor with practical efficiency makes BBD an integral part of improving accuracy in adsorption process optimization and sustainability in practice ensuring modified metal–organic frameworks (MOFs) function properly outside controlled environments. Therefore, it proves to be a powerful yet cost-effective solution grounded on scientific methodology for optimizing adsorption processes toward higher contaminant removal efficiencies.

The novelty of this study was presented a significant advancement through the creation of a distinctly engineered glutamic acid-functionalized Ag-MOF adsorbent that effectively integrates a high surface area, customized surface chemistry, and a selective affinity for Hg(II) ions. In contrast to previously documented adsorbents, this study incorporates glutamic acid as a dual-functional ligand with both amino and carboxyl groups, which considerably enhances coordination, chelation,

and electrostatic interactions with mercury ions, leading to superior adsorption capacity and selectivity. The synthesized NH_2-Ag-MOF not only features an exceptionally high surface area and a mesoporous pore structure but also showcases remarkable chemisorption properties and thermodynamic viability, as validated by both experimental and theoretical investigations. Additionally, the manuscript offers an extensive mechanistic analysis, underpinned by Density Functional Theory (DFT), which provides atomistic perspectives on Hg(II) ligand interactions an aspect that has not been previously explored for this category of modified Ag-MOFs. The incorporation of BBD for process optimization further establishes a statistically grounded approach that reduces the number of experimental trials while enhancing adsorption efficiency, thus representing a significant methodological improvement over traditional optimization technique. The adsorbent also demonstrates excellent regeneration capability and stability throughout multiple cycles. Collectively, these attributes position the proposed NH_2-Ag-MOF as an innovative and transformative material for the selective and sustainable remediation of Hg(II).

2. Experimental

2.1. Materials and instruments

Information concerning the materials and equipments can be found in the additional (Tables S1 and S2).[24–26]

2.2. Creation of adsorbent

2.2.1. Creation of Ag-MOF. A total of 1.64 g of 2-aminoterphtalic acid was dissolved in 25 mL of methanol, while 0.58 g of $AgNO_3$ was dissolved in 5 mL of bi-distilled water, resulting in the formation of silver metal–organic frameworks. Upon complete desolvation of the solutions, the anticipated hydrothermal synthesis protocol was employed to mix the solutions. The resultant mixture was subjected to heating in a Teflon autoclave with a capacity of 150 mL at a temperature of 90 °C for a duration of 20 hours, with a controlled heating rate of 5 °C per minute. Following the cooling process, the product was subjected to centrifugation and underwent four sequential washes with bidistilled water. The final step involved drying the material overnight at a temperature of 90 °C, as illustrated in Fig. 1.

2.2.2. Creation of NH_2-Ag-MOF. In the preparation of NH_2-Ag-MOF, a 1 : 1 molar ratio of silver-based metal–organic framework (Ag-MOF) to glutamic acid was incorporated into a mixture of dimethylformamide and ethylene glycol, followed by magnetic stirring for a duration of three hours at ambient temperature. The mixture was further processed in a Teflon autoclave, where it was heated for 20 hours at a gradual rate of 5 °C per min, reaching a temperature of 100 °C within a 150 mL capacity. After the heating phase, the solid powder of NH_2-Ag-MOF was allowed to cool and underwent four wash cycles with deionized water prior to centrifugation, followed by another overnight drying period at 90 °C, as depicted in Fig. 1.

2.3. Elimination and batch analysis of Hg(II) ions

The efficacy of NH_2-Ag-MOF as an adsorbent for the removal of Hg(II) ions was assessed using 25 mL conical tubes containing 0.1 g of the synthesized material, along with varied initial concentrations of Hg(II). The samples were subjected to agitation for 100 min at a rotational speed of 180 rpm within a shaking incubator. The pH levels were adjusted to a range between 1 and 7 utilizing 0.1 M HCl and/or NaOH. This investigation was conducted in a thermostatic shaking incubator to examine the adsorption isotherms, kinetics, and equilibrium parameters. In Fig. 1, a diverse array of initial Hg(II) concentrations (104–806 mg L^{-1}), adsorbent dosages (0.8–20 g L^{-1}), contact durations (5–100 min), and temperature conditions (20–45 °C) were employed in the experiments. Post-centrifugation at 9000 rpm, the analytical samples were evaluated using a PerkinElmer atomic absorption spectrometer. The sorption capacity of each sample was determined by averaging the results from three replicate experiments. The amount of Hg(II) adsorbed (q_e) and the removal percentage (% RE) were calculated according to eqn (1) and (2), respectively.

$$q_e = \frac{(C_0 - C_e)V}{M} \quad (1)$$

$$\%R = \frac{(C_0 - C_t)}{C_0} \times 100 \quad (2)$$

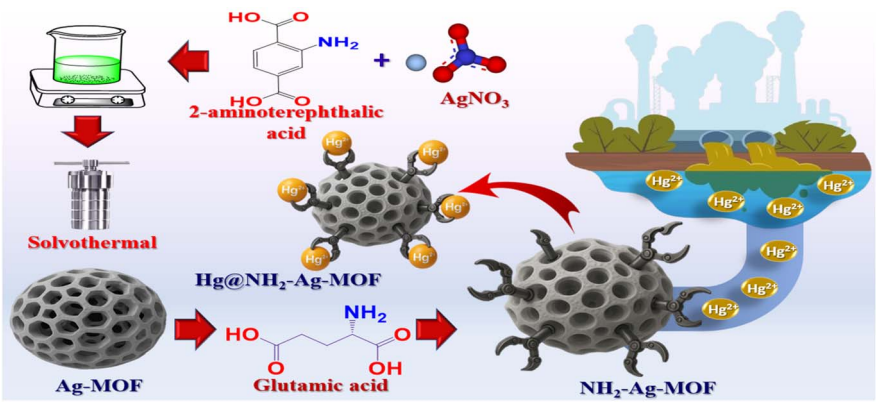

Fig. 1 Schematic illustration depicting the synthesis of NH_2-Ag-MOF and the subsequent removal of Hg(II) ions.

2.4. Experimental design

In scenarios characterized by multiple possible solutions, the Response Surface Methodology (RSM) technique is employed to develop numerical models. The primary objective of RSM is to establish the relationship between the response variable and the experimental factors, as well as to enhance the overall process. This methodology entails conducting a series of systematically organized experiments based on the characteristics of the process to determine the optimal solution. A commonly utilized approach for the optimization of process parameters is the central composite design (CCD). In this investigation, three operational variables were identified: "adsorbent weight", "contact duration", and "solution pH", as they were found to negatively impact adsorption efficiency (see Table S3).[27,28]

An exhaustive Table S3 was generated utilizing Design Expert Software, which delineates both the maximum and minimum values for each parameter under investigation. This table illustrates the diverse combinations of parameters alongside their respective results, encompassing "$2 \times m$" axial schemes, *P*-center schemes, and configurations involving "2^m" factorial experiments. The overall quantity of experimental trials, contingent upon the number of input variables, can be calculated using eqn (3).[29]

$$Np = [2^m + (2 \times m) + P] = [2^3 + (2 \times 3) + 3] = 17 \quad (3)$$

In this study, "*N*" represents the number of process parameters that influence the outcomes, while "*p*" refers to the number of experimental trials conducted. The value of "*m*" for the present investigation is noted to be 3. The central composite design encompasses three primary phases: the calculation of the model coefficients, the formulation of the experimental design, and the prediction of the model's performance in relation to the evaluation of results. Upon the completion of the process, an empirical model is constructed based on the collected data, allowing for an examination of how the objective functions with various adjustable input combinations. Consequently, a regression model in quadratic form is derived, as indicated in eqn (4).[30]

$$Y = \beta_o + \sum \beta_i X_i + \sum \beta_{ii} X_i^2 + \sum\sum \beta_{ij} X_i X_j \quad (4)$$

To exemplify, let us denote "*i*" as the variable representing "resistance" and "*j*" as the variable representing "speed". The parameters β_0, β_i, β_{ii}, and β_{ij} correspond to the individual influences of resistance, communication, speed, and the constant term, respectively. The efficacy of the proposed polynomial model was evaluated utilizing the metrics R^2, $R_{adj}{}^2$, and $R_{pred}{}^2$. A higher R^2 value signifies a formula that offers a superior fit to the experimental data.[31]

3. Results and discussion

3.1. Description of NH_2-Ag-MOF

3.1.1. X-ray diffraction patterns (XRD). The X-ray diffraction (XRD) patterns of NH_2-Ag-MOF are presented in Fig. 2. Our analysis, conducted using Foolproof and Check Cell equipment, indicates that the adsorbent structure is categorized within the P1 space group and exhibits a triclinic crystalline arrangement. Furthermore, our evaluations of the crystal dimensions yielded the following measurements: $a = 12.66$ Å, $b = 10.9$ Å, $c = 7.76$ Å, with angles $\alpha = 90°$, $\beta = 90°$, and $\gamma = 90°$. Detailed information regarding the interplanar spacing (d_{hkl}) and the Miller indices (*hkl*) for NH_2-Ag-MOF is available in Table S4. Moreover, the nanospheres comprising NH_2-Ag-MOF displayed significant stability in their crystalline structure, as evidenced by the persistence of their diffraction peak characteristics post-adsorption, as illustrated in Fig. 2.[32–34]

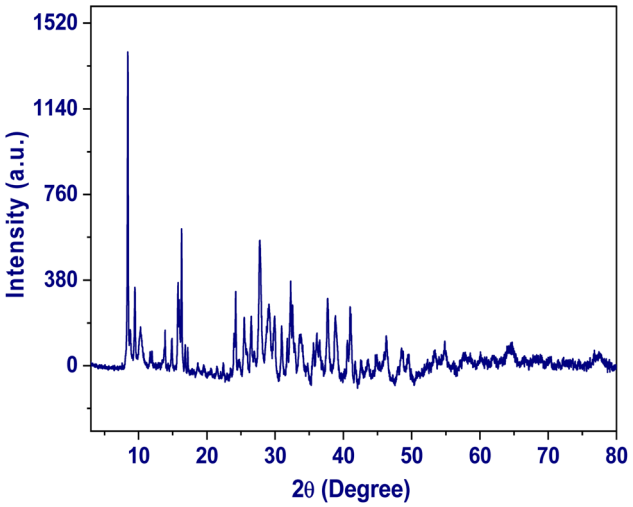

Fig. 2 XRD pattern of NH_2-Ag-MOF.

The X-ray diffraction (XRD) pattern of the synthesized material was evaluated utilizing QUALX software, with a comparison made to reference card no. 00-151-7611, which pertains to the crystalline phase $C_{54}H_{28}Ag_{16}N_{16}O_{38}$. The experimental diffractogram derived from the modified Ag-MOF demonstrates an exceptional alignment of peaks with the reference pattern, thereby confirming the effective retention of the parent Ag-MOF framework following its functionalization with glutamic acid. The prominent reflections throughout the 2θ range align precisely with the standard reference card, while the absence of extraneous diffraction peaks suggests that no secondary or impurity phases were formed during the modification process. Slight alterations in peak intensities and minor shifts in certain reflections are ascribed to the coordination of glutamic acid molecules *via* their amino and carboxylate moieties, which introduce electron-rich amine functionalities ($-NH_2$) and induce subtle structural modifications without detracting from the overall crystallinity of the material (Fig. S1(a)). These findings provide compelling evidence that the incorporation of glutamic acid was achieved in a manner that preserves the integrity of the Ag-MOF framework, while simultaneously enhancing the surface with amine groups, thereby corroborating the formation of the NH_2-Ag-MOF structure that is conducive to improved adsorption applications.[33,35]

The crystallographic parameters presented in Table 1 elucidate the relationship between the experimental X-ray diffraction

Table 1 Comparison of experimental X-ray diffraction peaks of NH_2-Ag-MOF with reference diffraction card 00-151-7611

Exp-2θ (°)	Exp-I (%)	Ref-2θ (°)	Ref-I (%)	d-Spacing (Å)	Match quality
8.43	1000.0	8.58	1011.6	10.48	Excellent
8.77	117.7	8.71	1.4	10.06	Good
9.45	248.4	9.63	3.9	9.35	Excellent
10.29	125.8	10.42	0.0	8.60	Very good
13.89	121.5	13.77	0.0	6.37	Very good
14.90	88.2	14.92	191.0	5.94	Excellent
15.78	271.3	15.76	0.8	5.61	Excellent
15.94	215.1	16.02	0.1	5.55	Excellent
16.31	433.5	16.44	0.3	5.43	Excellent
23.99	107.1	23.91	0.5	3.70	Excellent
24.23	242.4	24.21	0.4	3.67	Excellent
25.48	157.6	25.48	0.7	3.49	Perfect
26.50	160.5	26.51	0.0	3.36	Perfect
27.77	406.6	27.77	0.3	3.21	Perfect
28.76	187.0	28.75	1.0	3.10	Excellent
28.98	201.2	29.04	0.0	3.08	Very good
29.25	159.4	29.27	2.2	3.05	Excellent
29.94	168.2	29.95	3.9	2.98	Excellent
30.95	131.8	30.95	2.1	2.89	Perfect
31.81	90.3	31.82	0.0	2.81	Perfect
32.38	278.4	32.27	2.8	2.77	Excellent
32.56	194.5	32.54	0.0	2.75	Excellent
33.61	99.0	33.61	6.3	2.66	Perfect

(XRD) profile of the synthesized NH_2-Ag-MOF and the established diffraction data for Ag-MOF, as denoted by PDF card no. 00-151-7611. The strong alignment of the prominent diffraction peaks, particularly at $2\theta = 8.43°$, 9.45°, 15.78°, 23.99°, 25.48°, 26.50°, and 27.77°, with their corresponding reference reflections corroborates that the fundamental structure of the Ag-based metal–organic framework is largely conserved following the modification with glutamic acid. The significant retention of these peaks suggests that the introduction of $-NH_2$ functional groups does not disrupt the crystallographic arrangement of the original framework, thereby sustaining its inherent coordination environment. The observed minor variations in peak intensities and slight shifts within the angular range of 28°–33° further reinforce the successful integration of glutamic acid, which leads to localized lattice distortions and the establishment of additional Ag–N and Ag–O coordination interactions, all while maintaining the overall structural coherence. The lack of extraneous reflections coupled with the presence of only a limited number of unindexed peaks at elevated angles confirms that no secondary crystalline phases or impurity products were generated during the modification process. Taken together, these observations affirm that the functionalization approach effectively preserves the crystallinity of the Ag-MOF framework while introducing amino-rich surface sites, thus rendering the NH_2-Ag-MOF a stable and structurally coherent platform with an enhanced capacity for heavy-metal adsorption.

The X-ray diffraction refinement profile generated through the Profex software offers substantial evidence regarding both the structural stability and the successful functionalization of the synthesized NH_2-Ag-MOF. The experimental diffraction pattern obtained aligns exceptionally well with the calculated diffraction pattern, signifying that the crystallographic model utilized effectively captures the atomic arrangement within the material. The slight discrepancies observed between the measured and calculated intensities, as indicated by the nearly horizontal difference line, suggest a high-quality match and the absence of unrecognized crystalline contaminants. Moreover, the deconvolution of the diffraction peaks allows for the identification of specific elemental contributions, with distinct reflections associated with silver (Ag), carbon (C), and nitrogen–oxygen species clearly discerned (Fig. S1(b)). The presence of Ag reflections serves as confirmation for the incorporation of metallic silver nodes within the metal–organic framework (MOF), while the carbon and N–O peaks substantiate the presence of the organic ligand backbone along with the successful introduction of amino functionalities derived from glutamic acid. This elemental analysis directly reinforces the integrity of the Ag-MOF coordination network and the establishment of NH_2-modified sites without compromising the original structural order. Collectively, the results obtained from the Profex refinement substantiate the findings from QualX and conclusively demonstrate that the synthesized NH_2-Ag-MOF maintains its crystalline characteristics while integrating nitrogen-rich functional groups critical for improved adsorption performance.[36]

3.1.2. Brunauer–Emmett–Teller (BET) surface area. The nitrogen adsorption–desorption isotherm analysis of NH_2-Ag-MOF reveals a considerable surface area of 1750.49 $m^2\ g^{-1}$, characterized by a mesoporous pore diameter of 3.84 nm and a pore volume of 3.38 $cm^3\ g^{-1}$ (Fig. 3(a)).[37] These properties render the material highly effective for the adsorption of heavy metals, particularly Hg(II). The elevated surface area provides an abundance of adsorption sites, while the mesoporous architecture, with its optimal pore dimensions, facilitates the efficient ingress of Hg(II) ions into the material's framework. Furthermore, the presence of silver (Ag) ions and amine (NH_2) groups contributes to improved selectivity and adsorption efficiency through the promotion of specific interactions with Hg(II) species. The Type IV isotherm exhibits pronounced hysteresis at higher relative pressures, corroborating the mesoporous nature of the material and indicating the phenomenon of capillary condensation (see Fig. 3(b)). These results substantiate the material's suitability for environmental remediation initiatives aimed at the extraction of hazardous heavy metals.[38]

3.1.3. FT-IR. Fig. 3(c) of the FTIR spectrum illustrated a variety of functional groups and chemical bonds present within the NH_2-Ag-MOF structure. The broad band occurring at approximately 3332 cm^{-1} is most likely attributed to the O–H bond. The band observed at 1233 cm^{-1} is primarily due to the stretching and bending vibrations of the N–H bond, specifically from the $-NH_2$ groups located on the surface of the NH_2-Ag-MOF. The presence of carboxyl functional groups was confirmed as the origin of the C=O bond vibrations, which resulted in a pronounced band at 1571 cm^{-1}. Furthermore, the NH_2-Ag-MOF exhibited a C–OH vibration at 1416 cm^{-1} and a C–H saturated bond at 3056 cm^{-1}. The Ag–O bond vibration in

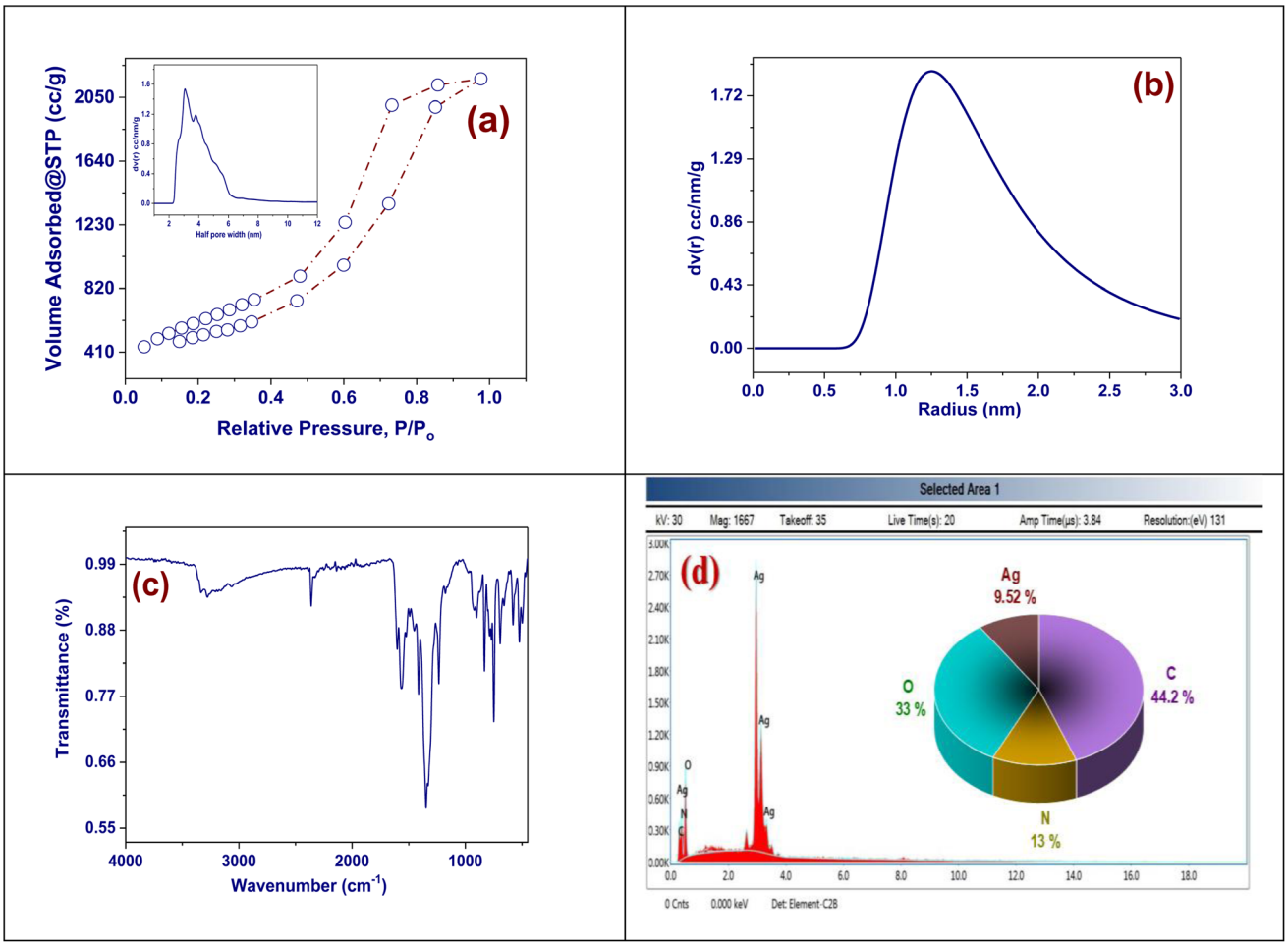

Fig. 3 Characterization of NH_2-Ag-MOF: (a) N_2 adsorption–desorption isotherm, (b) distribution of pore radius, (c) FT-IR spectrum, and (d) EDX analysis.

the NH_2-Ag-MOF was identified in the band at 514 cm^{-1}. The FTIR analysis indicates a diverse array of oxygen and nitrogen functional groups present in the synthesized NH_2-Ag-MOF. These functional groups are critical for the effective adsorption of heavy metal ions, serving as pivotal sites for this process.[39]

3.1.4. EDX analysis. The Energy-Dispersive X-ray Spectroscopy (EDX) profile illustrated in Fig. 3(d) corroborates the successful synthesis and elemental composition of the NH_2-Ag-MOF. The spectrum exhibits prominent peaks associated with silver (Ag), thereby affirming its role as the central metallic node within the framework. Quantitative analysis reveals that Ag comprises 9.52% of the total material, indicating that the functional modification process preserved the metal content. The substantial signals of carbon (C, 44.2%), oxygen (O, 33%), and nitrogen (N, 13%) further substantiate the integration of the organic linker and the amine functionality introduced through glutamic acid. The significant percentages of carbon and oxygen stem from the aromatic and carboxylate groups present in the organic ligand, while the detectable nitrogen confirms the effective grafting of $-NH_2$ groups onto the surface of the MOF. This nitrogen-rich functionality is imperative for enhancing adsorption affinity for Hg(II) *via* chelation and complexation mechanisms. Furthermore, the uniform distribution of elements and the absence of extraneous peaks indicate the purity of the synthesized NH_2-Ag-MOF, confirming that no undesirable impurities or secondary phases were generated during synthesis.[40] Consequently, this EDX analysis reinforces the structural and compositional evidence that the NH_2-Ag-MOF framework is effectively functionalized and chemically optimized for selective mercury adsorption.[41,42]

3.1.5. SEM analysis. The FESEM images presented in Fig. 4 provide a comprehensive illustration of the distinctive morphological features and elemental uniformity of the synthesized NH_2-Ag-MOF. This morphology suggests the presence of significant porosity and a substantial accessible surface area conducive to the diffusion and adsorption of metal ions. The irregular and textured topography observed is indicative of well-structured metal–organic frameworks (MOFs), thus confirming that the synthesis methodology effectively yielded a highly porous and interconnected framework rather than consolidated crystalline aggregates. The accompanying elemental mapping serves to reinforce the consistent distribution of the primary framework components carbon, nitrogen,

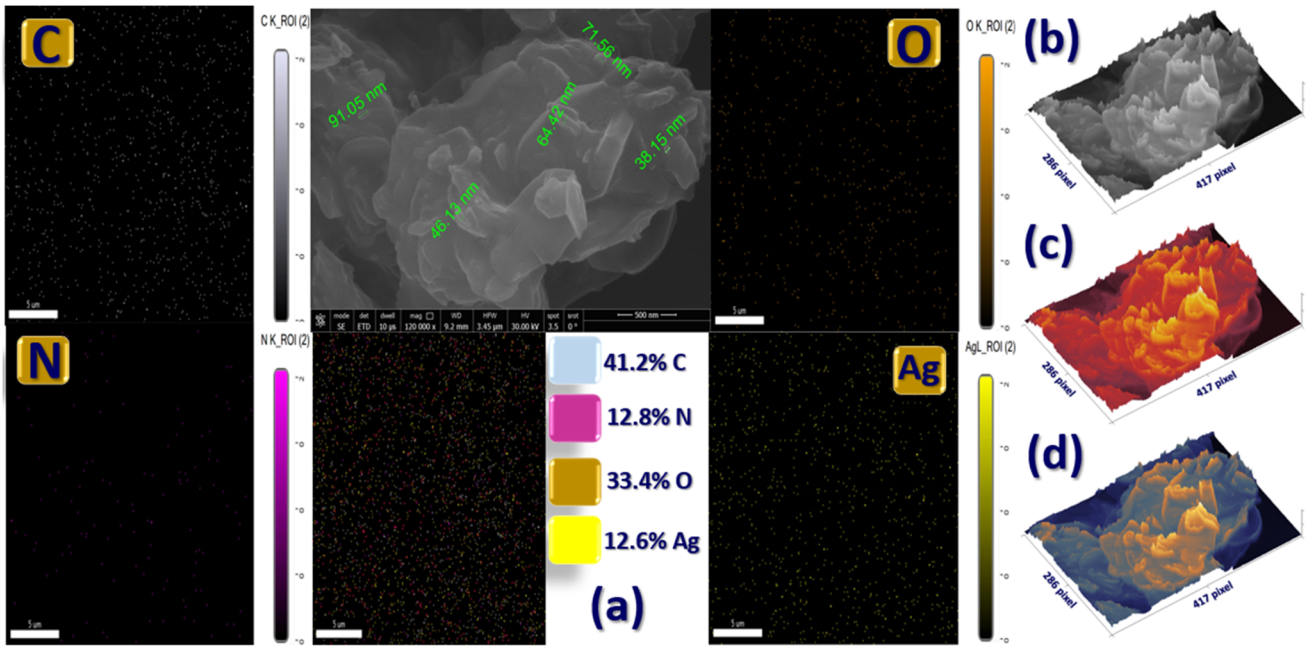

Fig. 4 FESEM images of NH_2-Ag-MOF: (a) SEM mapping, (b) grayscale, (c) thermal color, (d) cool blue tones.

oxygen, and silver throughout the surface of the material. In this context, carbon is primarily linked to the organic linker backbone, while nitrogen confirms the successful incorporation of amine groups resulting from glutamic acid functionalization. The presence of oxygen is attributed to carboxylate groups that play a role in metal coordination, and the silver is identified as the central metal nodes stabilizing the MOF architecture. The quantitative elemental mapping results show compositions of 41.2% carbon, 12.8% nitrogen, 33.4% oxygen, and 12.6% silver, which correspond closely to the anticipated chemical formula, suggesting that no foreign phases or contaminants were introduced during the synthesis.[43] The concurrent presence and homogeneous dispersal of these four elements further validate the structural integrity and chemical consistency of the NH_2-Ag-MOF, emphasizing its well-defined framework and the prevalence of functional sites that can effectively interact with Hg(II) ions. This interaction significantly enhances its adsorption selectivity and overall performance (Fig. 4(a)). The visual representations in grayscale (Fig. 4(b)), thermal color (Fig. 4(c)), and cool-tone projections collectively illustrate a layered nanosheet-like structure characterized by folded and wrinkled formations (Fig. 4(d)).

3.1.6. XPS analysis. The high-resolution X-ray photoelectron spectroscopy (XPS) data for the Ag 3d region of Ag-MOF-NH_2, before and after Hg(II) ion adsorption (Hg@Ag-MOF-NH_2), provide insights into the interactions between mercury ions and the amine-functionalized silver sites. In the unaltered Ag-MOF-NH_2 XPS spectrum, Ag $3d_{5/2}$ and Ag $3d_{3/2}$ signals appear at binding energies of about 368.32 and 374.65 eV, representing the typical oxidation state of silver. The peak positioning and a separation of approximately 6.3 eV between the spin–orbit doublets indicate that silver is mainly in the Ag^+ coordination sphere, stabilized by the organic linker matrix. After Hg(II) adsorption, shifts are observed in the peaks for Ag $3d_{5/2}$ and Ag $3d_{3/2}$ to lower binding energies (368.11 and 374.09 eV), along with changes in peak intensity and area distribution.[44] These alterations imply strong electronic interactions between silver sites and Hg(II), suggesting partial electron transfer and coordination between mercury and the amine functional groups. The decrease in binding energies corresponds to changes in the local electronic environment around the silver atoms due to Hg(II) complexation, indicating that adsorption involves chemical bonding rather than just physical interaction. Additional fitted components and variations in peak ratios validate Ag–N–Hg coordination interactions, highlighting the role of amine groups in facilitating selective mercury capture. Overall, the XPS findings confirm that Hg(II) adsorption onto Ag-MOF-NH_2 occurs through a chemisorptive mechanism with direct interactions and electronic perturbations at the Ag coordination center, showcasing the material's affinity and selectivity for mercury ions (Fig. 5).

The high-resolution C 1s XPS spectra for NH_2-Ag-MOF and Hg@NH_2-Ag-MOF provide insights into the chemical environment of carbon before and after Hg(II) adsorption. The unmodified NH_2-Ag-MOF spectrum shows a primary C 1s peak deconvoluted into three components: one at 284.21 eV (C–C/C–H bonds from the aromatic organic linker), another at 285.93 eV (C–N/C–O species from the amine-functionalized ligand), and a peak at 288.56 eV (O═C–O groups from carboxylates coordinating with silver centers). The peak intensities confirm successful integration of amine and carboxyl functionalities. After Hg(II) adsorption, significant changes in the XPS profile of Hg@NH_2-Ag-MOF are observed. The C–C/C–H component remains dominant, but shifts in the C–N/C–O peak and an increase in the O═C–O contribution indicate electronic perturbation from mercury binding. The increase in the

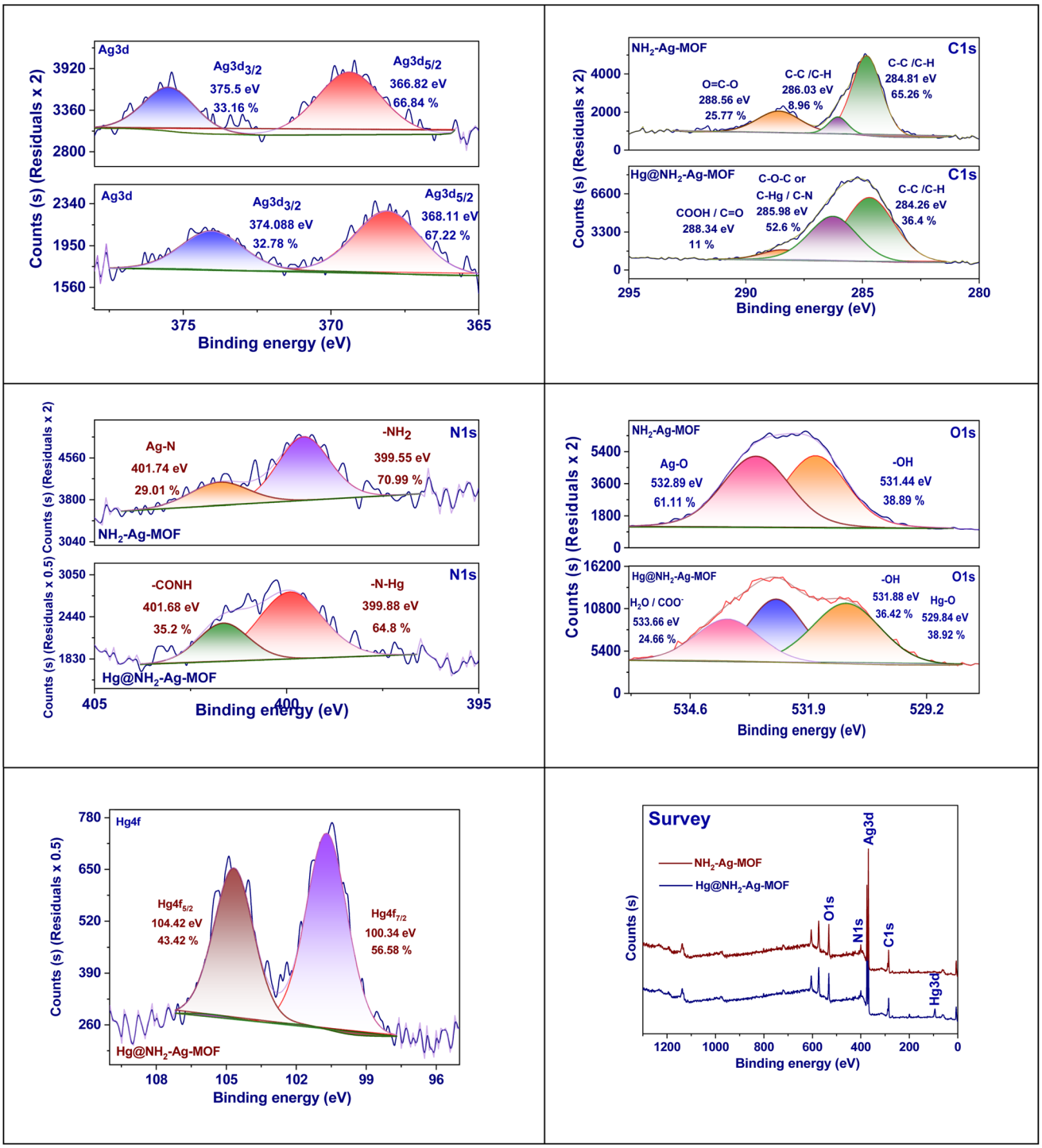

Fig. 5 XPS analysis of NH_2-Ag-MOF.

carboxylate peak intensity suggests mercury ions preferentially interact with nitrogen and oxygen donor sites, promoting complexation over physical adsorption.[45–47] These shifts reflect a redistribution of electron density consistent with a coordination-driven adsorption mechanism, where Hg(II) interacts closely with amine and carboxylate functionalities. This analysis highlights the organic linker's crucial role in Hg(II) immobilization, supporting the idea that adsorption is facilitated by strong chemisorptive interactions in the NH_2-modified framework.

The N 1s XPS spectra in Fig. 5 reveal critical insights into the nitrogen chemical states in NH_2-Ag-MOF and how they change upon Hg(II) adsorption. The unaltered NH_2-Ag-MOF shows a N 1s peak split into two parts: 400.11 eV relates to Ag–N coordination bonds between silver nodes and nitrogen ligands, while 399.55 eV represents unbound –NH_2 groups in the framework.

This intensity distribution confirms both coordinated and uncoordinated nitrogen sites, indicating that amine groups partly participate in metal–ligand interactions, retaining available binding sites. After introducing mercury, the N 1s profile for Hg@NH_2-Ag-MOF shows notable changes, including an additional peak at 402.11 eV, highlighting the formation of new nitrogen–mercury coordination complexes. The relative intensity of the –NH_2 peak declines, and there is a partial decrease in the Ag–N component, suggesting the involvement of free amine nitrogen in bonding with Hg(II). The shift to higher binding energies and increased intensity of the N–Hg peak suggest electron withdrawal from nitrogen during complexation, indicating a chemisorptive mechanism. These spectral alterations underscore nitrogen's role as a key coordination site for Hg(II), emphasizing the importance of amine groups in enhancing both adsorption affinity and selectivity. Thus, N 1s XPS analysis verifies that mercury capture occurs *via* strong N–Hg interactions, enriching the understanding of Hg(II) immobilization in the NH_2-functionalized Ag-MOF framework.

The O 1s XPS spectra for NH_2-Ag-MOF and Hg@NH_2-Ag-MOF reveal insights into oxygen-containing functional groups and their relation to Hg(II) coordination. In NH_2-Ag-MOF, the O 1s spectrum shows two main peaks: 531.48 eV for O–H groups linked to surface hydroxyls and 532.89 eV for Ag–O bonds, confirming coordination of oxygen from carboxylate ligands to silver centers. The relative intensities indicate a significant amount of oxygen in a coordinated state, supporting its role in stabilizing the metal–ligand framework. Following Hg(II) adsorption, the O 1s profile of Hg@NH_2-Ag-MOF changes notably, with a new peak at 533.41 eV attributed to C=O/O–C=O groups involved in metal–carboxylate complexation, signaling Hg–O interactions. Simultaneously, intensities for Ag–O and O–H decrease, indicating these oxygen atoms participate in binding Hg(II) ions. Increased contributions at higher binding energies imply electron density withdrawal due to Hg(II) coordination, confirming strong chemisorptive interactions over mere physical adsorption.[45–47] These changes highlight that oxygen-based moieties, particularly carboxylate groups, serve as key anchoring sites for mercury immobilization, enhancing nitrogen coordination and the mechanisms for capturing Hg(II) with NH_2-Ag-MOF.

The high-resolution Hg4f XPS spectrum of Hg@NH_2-Ag-MOF provides clear evidence of mercury incorporation into the framework. The spectrum displays two peaks corresponding to the Hg(II) spin–orbit doublets: Hg $4f_{7/2}$ and Hg $4f_{5/2}$, at binding energies of 100.34 and 104.42 eV, respectively, with an energy separation of about 4.08 eV, aligning with expected spin–orbit splitting for divalent mercury. These peaks confirm successful integration of Hg(II) ions into the NH_2-Ag-MOF surface instead of a solvated state. The significant intensity of the $4f_{7/2}$ peak, making up 56.26% of the total intensity, indicates that mercury is mainly adsorbed in its oxidized form. The fitted envelope reveals secondary contributions from chemical interactions, emphasizing the role of nitrogen and oxygen groups in binding mercury. The lack of peaks for metallic mercury or mixed valence states suggests adsorption occurs *via* complexation rather than reduction. These spectral traits affirm effective immobilization of Hg(II) within NH_2-Ag-MOF, supporting the chemisorptive nature of the adsorption as demonstrated by thermodynamic and kinetic studies, enhancing the understanding of the modified framework's role in selective, stable mercury capture.[48]

3.1.7. Thermal gravimetric analysis (TGA). The NH_2-Ag-MOF TGA shows a clear multi-step thermal decomposition profile, confirming good structural stability and successful functionalization. The first weight loss of ~14.3% between ~26 to 170 °C is due to the removal of physically adsorbed water and trapped solvent molecules within its porous framework. This is followed by a second stage between ~235 to 341 °C with weight loss of about 17.5% corresponding to coordinated solvents' release and partial decomposition of surface functional groups particularly amine (–NH_2). More pronounced degradation starts at around ~292 to 411 °C as indicated by DTG peaks which means that the organic linker is progressively breaking down. Major structural collapse takes place from ~424 to 554 °C with significant weight loss about 27.4% which has been assigned to complete decomposition of the organic framework plus destruction of MOF architecture supported by a strong DTG peak around ~485 °C plus corresponding DTA signals; only minor mass changes are observed beyond ~600 °C indicating the formation of thermally stable inorganic residues such as silver or silver oxide (Fig. S2). In summary, NH_2-Ag-MOF presents significant thermal stability up to about 300 °C, which confirms its eligibility for adsorption application under moderate thermal conditions and emphasizes the toughness of its framework before degradation.[49]

3.1.8. Zero point of charge (pH_{zpc}). The pH_{zpc} of the NH_2-Ag-MOF was assessed utilizing the ΔpH *versus* initial pH approach, as demonstrated in Fig. 6(a). The ΔpH values initially exhibit an increase at lower solution pH levels, ultimately crossing the zero line at a pH of 2.7. This observation indicates that at this pH, the surface of the NH_2-Ag-MOF possesses a net neutral charge. Below this threshold (pH < 2.7), the ΔpH values are positive, which signifies the protonation of amino and carboxylate groups present on the surface of the MOF, resulting in a positively charged adsorbent. Consequently, this condition leads to electrostatic repulsion between the positively charged surface of the NH_2-Ag-MOF and cationic mercury (Hg(II)) species (Hg^{2+} and $HgOH^+$), thereby decreasing the adsorption efficiency. Once the pH exceeds the pH_{zpc} of 2.7, the ΔpH values turn negative, indicating the deprotonation of amine groups and the progressive establishment of a negative surface charge. This deprotonation process promotes electrostatic attraction and coordination interactions with Hg(II) ions, thereby facilitating their uptake through complexation with the surface –NH_2 and –O functional groups. Hence, the pH_{zpc} value of 2.7 substantiates that the NH_2-Ag-MOF surface becomes more conducive to Hg(II) adsorption at pH levels above 2.7, which corresponds with the experimentally recorded enhancement in removal capacity under mildly acidic to near-neutral conditions. These findings underscore the critical role of surface charge development in influencing the adsorption mechanism and the affinity of NH_2-Ag-MOF towards Hg(II) ions.

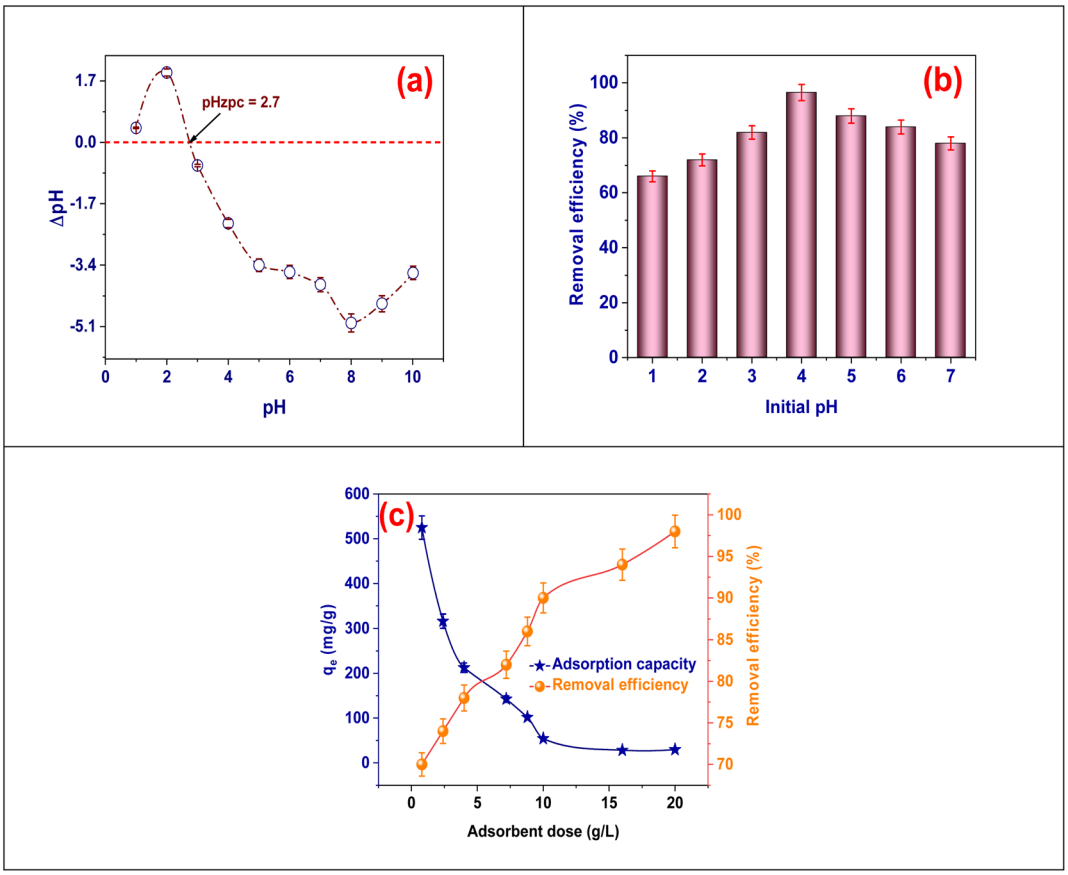

Fig. 6 (a) Resolve of zero point of charge of NH_2-Ag-MOF, (b) impact of pH (pH: 1 to 7, C_i: 200 mg L^{-1}, dose: 0.02 g, contact time: 100 min, volume 25 mL, temperature 25 °C), (c) impact of adsorbent dose (pH: 4, C_i: 600 mg L^{-1}, dose: 0.02 to 0.50 g, contact time: 100 min, volume 25 mL, temperature 25 °C).

3.2. Batch experiments

3.2.1. Effect of pH. The effect of initial pH on the adsorption efficacy of Hg(II) by NH_2-Ag-MOF, illustrated in Fig. 6(b), exhibits a distinct pH-dependent response, with optimal removal observed at a pH of 4.0, notably exceeding the material's point of zero charge ($pH_{zpc} = 2.7$). At pH levels below 2.7, the NH_2-Ag-MOF surface bears a positive charge due to the protonation of amino and oxygen-containing functional groups, which induces significant electrostatic repulsion against the cationic Hg(II) ions, consequently limiting removal efficiency in this acidic range. As pH levels rise above the pH_{zpc}, the surface gradually develops a negative charge through the deprotonation of the $-NH_2$ groups, thereby considerably enhancing electrostatic attraction and coordination interactions with Hg(II).[50–52] This transformation from a positively charged to a negatively charged surface elucidates the pronounced increase in adsorption efficiency, peaking at pH 4.0, where a combination of plentiful negatively charged active sites and partially hydrolyzed Hg(II) species promotes robust complexation and surface binding.[53] Beyond pH 4.0, a moderate decrease in removal efficiency may be due to competition with hydroxide ions and the incrementally occurring conversion of Hg(II) into neutral or negatively charged hydroxo complexes.[54,55] Thus, the optimal functionality at pH 4.0 underscores that efficient adsorption transpires under conditions where the adsorbent surface is negatively charged and Hg(II) remains in an easily bindable cationic state, highlighting the pivotal role of surface charge modulation in relation to the pH_{zpc} of NH_2-Ag-MOF.[56]

3.2.2. Adsorbent dose. The influence of NH_2-Ag-MOF dosage on the adsorption of Hg(II) ions demonstrates a significant pattern in which the adsorption capacity diminishes concurrently with an increase in removal efficiency as the concentration of the adsorbent escalates.[57] At a lower dosage of 0.8 g L^{-1}, the adsorbent shows its peak adsorption capacity of 525 mg g^{-1}, a phenomenon attributed to the competitive interaction of Hg(II) ions vying for a limited pool of active sites. Nonetheless, the overall removal efficacy at this dosage remains moderate at 70%, owing to an insufficient surface area to accommodate the total Hg(II) ions present (Fig. 6(c)). As the dosage is raised to 2.4, 4, and 7.2 g L^{-1}, the availability of additional functional sites, such as $-NH_2$ and Ag-coordination centers, enhances the interactions and binding affinities with Hg(II), thereby increasing the removal efficiencies to 74, 78, and 82%, respectively, despite a reduction in adsorption capacities to 316.4, 212.62 and 142.4 mg g^{-1}. This reduction can be explained by the situation where the number of active sites surpasses the availability of mercury ions, leading to

suboptimal utilization of the adsorbent surface. At elevated dosages, specifically 16 and 20 g L^{-1}, the adsorption capacities further decrease to 28.12 and 29.4 mg g^{-1}; however, the removal efficiencies ascend to almost complete elimination levels of 94 and 98%, respectively. These findings elucidate that NH_2-Ag-MOF retains a remarkable affinity for Hg(II), indicating that even minimal quantities can effectively adsorb considerable amounts of mercury, while larger dosages facilitate nearly complete purification processes. This dual behavior reinforces the efficacy, selectivity, and economic viability of NH_2-Ag-MOF as an advanced adsorbent for the remediation of mercury in aqueous systems (Fig. 6(c)).

3.3. Adsorption isotherm

The impact of initial Hg(II) concentration on the adsorption efficacy of NH_2-Ag-MOF reveals a concentration-dependent trend characterized by an increase in adsorption capacity, while removal efficiency exhibits a gradual decline with rising metal concentration. At lower initial concentrations, such as 104.2 mg L^{-1}, the availability of Hg(II) ions is relatively low in comparison to the plentiful active sites present on the NH_2-Ag-MOF surface. This abundance facilitates efficient binding, resulting in a high removal efficiency of 94.44%. However, the adsorption capacity remains moderate at 119.39 mg g^{-1} due to the limited availability of ions. As the concentration escalates, a pronounced concentration gradient propels a greater number of Hg(II) ions toward the adsorbent surface, which enhances interaction and coordination with the amino groups and silver centers incorporated within the MOF structure. Consequently, this interaction markedly increases the adsorption capacity, reaching values of 296.56, 474.27 mg g^{-1}, and ultimately 636.27 mg g^{-1} at an initial concentration of 806.60 mg L^{-1}. Nonetheless, despite the significant augmentation in adsorption capacity, the removal efficiency progressively decreases from over 94% to approximately 63%. This decline occurs due to the saturation of the finite number of adsorption sites, which limits their ability to accommodate all Hg(II) ions present at higher concentrations, thereby resulting in a greater proportion of ions remaining unadsorbed in the solution. The simultaneous rise in adsorption capacity alongside the decrease in removal efficiency underscores that NH_2-Ag-MOF possesses a high affinity and considerable loading capability, even at elevated levels of contaminants. These characteristic underscores its considerable potential for the treatment of mercury-laden industrial effluents, where elevated metal concentrations necessitate resilient adsorbent performance (Fig. S3(a)).

Important details regarding the adsorption of Hg(II) ions on NH_2-Ag-MOF are provided by adsorption isotherm models. The models, such as Freundlich and Langmuir,[58] determine the best adsorption capability and provide a clear picture of the amount of Hg(II) that the NH_2-Ag-MOF can adsorb at equilibrium.[59] This information is essential for evaluating its effectiveness and potential for use in practical applications. Adsorption on surfaces with changes is classified as either single-layer or multi-layer under the Langmuir and Freundlich models.[59] These models provide insight into how mercury ions interact with MOF surfaces, whether uniformly or differently. Models like Freundlich and Dubinin–Radushkevich have parameters that give important information about the extent and feasibility of adsorption.[60] They can show whether the interactions are physical or chemical, helping researchers to tailor conditions for optimal efficiency.[61] These models can also predict the response of Hg(II) adsorption to varying concentrations and environmental conditions, simulating real-world applications and ensuring practical field outcomes.[62] They also assist in maximizing the efficiency of NH_2-Ag-MOF usage for removing mercury, reducing excessive use of the adsorbent and preserving resources. Through the examination of how Hg(II) ions interact with the amino and silver sites on NH_2-Ag-MOF, isotherms provide insight into the specific dynamics of these interactions, including electrostatic attractions and coordination bonds. This contributes to the adsorbent's selectivity and performance.[61] Adsorption isotherms offer a way to compare NH_2-Ag-MOF's performance with other adsorbents, helping researchers select the most effective material for removing mercury in wastewater treatment. Essentially, isotherm models provide a systematic representation of capacity, binding dynamics, favorability, and performance, which are essential for optimizing NH_2-Ag-MOF for effective Hg(II) adsorption as shown in Table S5.

By highlighting the adsorption capacity and the nature of the connections, the model of Langmuir adsorption isotherm is crucial for understanding Hg(II) adsorption on NH_2-Ag-MOF. According to this model, adsorption occurs in a monolayer on a consistent surface, with each mercury ion taking up a specific location on NH_2-Ag-MOF. This makes the model ideal for illustrating the maximum capacity for adsorption.[58] With a maximum adsorption capability q_e of 638.2 mg g^{-1}, the NH_2-Ag-MOF has a high ability to effectively collect mercury ions. This is important for practical uses in removing heavy metals. The Langmuir constant K_L, which is determined to be 0.0207 L mg^{-1}, indicates the relationship between the adsorbent and Hg(II). A moderate value implies a reasonable binding strength that is necessary for efficient removal of Hg(II) without excessive use of material. The R_L value of 0.48 indicates favorable adsorption, falling between 0 and 1, and suggesting efficient adsorption of mercury at various concentrations (Fig. 7(a and b)). This indicates that NH_2-Ag-MOF can effectively perform under different conditions.[58] In summary, the Langmuir model's parameters q_e, K_L, and R_L provide a comprehensive and quantitative insight into NH_2-Ag-MOF's ability to adsorb, such as its maximum capacity and favorability. These parameters also enable comparison with other adsorbents. This methodical process not only improves NH_2-Ag-MOF's effectiveness in removing mercury, but also enables easy expansion in treating wastewater. It shows how Langmuir modeling can offer useful direction for achieving efficient, focused adsorption solutions as demonstrated in Table S6.

The process by which Hg(II) is adsorbed onto NH_2-Ag-MOF can be better understood using the adsorption isotherm model of Freundlich.[59] It can be used to depict adsorption on surfaces with different affinities, unlike the Langmuir model, which assumes homogenous adsorption places. The Freundlich

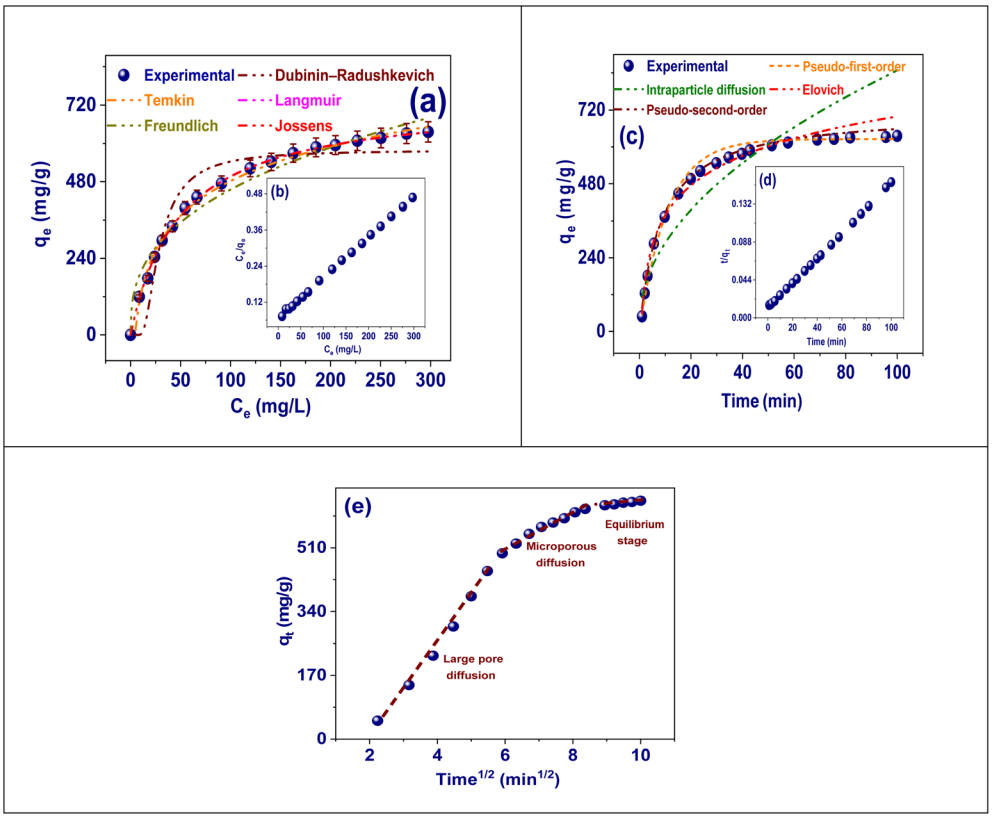

Fig. 7 (a) Adsorption isotherm models (pH: 4, C_i: 104 to 806 mg L^{-1}, dose: 0.02 g, contact time: 100 min, volume 25 mL, temperature 25 °C), (b) Langmuir linear model, (c) adsorption kinetic models (pH: 4, C_i: 500 mg L^{-1}, dose: 0.02 g, contact time: 100 min, volume 25 mL, temperature 25 °C), (d) pseudo-second-order linear form, and (e) diffusion mechanism of Hg(II) onto NH_2-Ag-MOF (pH: 4, C_i: 500 mg L^{-1}, dose: 0.02 g, contact time: 100 min, volume 25 mL, temperature 25 °C).

model is more appropriate for relating the heterogeneity of NH_2-Ag-MOF's surface, where mercury ions can bind to sites with varying binding energies. The Freundlich constant K_F of 83.7 (mg g^{-1}) (L $mg^{-1})^{1/n}$ shows that NH_2-Ag-MOF has a great adsorption capacity for mercury under different conditions. Additionally, the computed constant n of 2.72 provides us with information regarding the favorability and intensity of the adsorption procedure. When the value of n exceeds 1, the procedure becomes advantageous, indicating that NH_2-Ag-MOF has the ability to efficiently capture mercury ions, even with increasing concentration.[44,63] This suggests that adsorption is more focused at higher initial concentrations, which can be beneficial for treating wastewater with varying levels of mercury. The Freundlich model's capacity to illustrate multilayer adsorption on a heterogeneous surface offers a more realistic view of the interactions between Hg(II) ions and NH_2-Ag-MOF's functional groups, such as amino and silver sites, which may vary in their binding strengths.[59] This flexibility in the model offers predictive insights for scaling, as it suggests NH_2-Ag-MOF can handle fluctuations in mercury concentration effectively. Overall, the Freundlich model's parameters, K_F and n, offer a comprehensive picture of NH_2-Ag-MOF's adsorption capacity, efficiency, and adaptability, making it highly useful for optimizing mercury removal processes in dynamic wastewater conditions (Fig. 7(a and b)).

Significant details on the adsorption of Hg(II) onto NH_2-Ag-MOF can be found using the Dubinin–Radushkevich (D–R) adsorption isotherm model. This model analyzes factors such as adsorption capacity, strength, and mechanisms, allowing for a distinction between physical and chemical adsorption. In contrast to Langmuir and Freundlich models, the D–R model provides a more comprehensive insight into adsorption energetics, essential for assessing the stability of mercury adsorption on NH_2-Ag-MOF.[60] Boasting a maximum adsorption capability Q_{DR} of 578.88 mg g^{-1}, this model verifies NH_2-Ag-MOF's efficacy in capturing and retaining Hg(II) ions, demonstrating its appropriateness for widespread use in mercury removal applications. The D–R constant K_{DR} of 1.04 × 10^{-4} mol^2 kJ^{-2} and the calculated average adsorption energy E_a of 31.6 kJ mol^{-1} provide additional support for this analysis. An E_a value greater than 20 kJ mol^{-1} indicates chemisorption rather than physisorption.[64] This is highly beneficial for treating wastewater, since chemisorption results in a more robust and enduring attachment of Hg(II) ions, leading to a decreased risk of mercury being released back into the environment. The D–R model also provides insight into how NH_2-Ag-MOF interacts with specific functional groups like amino and silver sites, indicating that it is likely to form strong chemical bonds with mercury. This enhances the material's ability to capture and retain mercury selectively. By evaluating adsorption at different

concentrations, the D–R model can better adjust to real-life situations, considering the diversity in wastewater compositions. In combination, the Q_{DR}, K_{DR}, and E_a parameters obtained from the D–R model provide a comprehensive understanding into the adsorption efficiency, mechanism, and stability of NH_2-Ag-MOF, making this model essential for optimizing NH_2-Ag-MOF for effective and long-lasting elimination of mercury in wastewater treatment procedures.

By taking into account the connections among the mercury ions and the adsorbent surface during adsorption, the Temkin adsorption isotherm model helps explain how Hg(II) is adsorbed onto NH_2-Ag-MOF. This differs from other models that assume a constant energy level across sites. The Temkin model suggests that as surface coverage increases, the adsorption energy of NH_2-Ag-MOF active sites decreases in a linear fashion.[61] This reflects a more accurate representation of the scenario where occupied active sites become less energetically favorable. The Temkin constant b_T of 15.84 J mol^{-1} for NH_2-Ag-MOF indicates a moderate binding energy for Hg(II), implying a favorable yet not overly strong interaction. The equilibrium between effectiveness and reversibility is advantageous for applications requiring efficient yet somewhat reversible adsorption, particularly when there is a need for adsorbent regeneration. Moreover, the equilibrium binding constant K_T of 0.22 L mol^{-1} demonstrates a strong affinity for Hg(II), indicating that NH_2-Ag-MOF can effectively capture mercury ions from the solution. The Temkin isotherm effectively represents the varying adsorption energy with coverage, given the heterogeneous surface properties of NH_2-Ag-MOF. This is due to the diverse connections among different useful groups (such as amino and carboxy sites) and Hg(II) ions. The Temkin model's flexibility makes it an effective tool for evaluating how adsorption behaves in situations of high substance concentration. This is particularly useful for treating wastewater, where mercury levels can fluctuate.[65] In summary, the Temkin model's parameters b_T and K_T offer valuable information about NH_2-Ag-MOF's ability to adsorb, its effectiveness, and its flexibility in varying conditions. This makes it a suitable option for improving mercury removal processes that need a thorough understanding of adsorption patterns over time.[61]

A useful model for describing the procedure of Hg(II) adsorption on NH_2-Ag-MOF is the Jossens adsorption isotherm model. It is helpful since it can consider the surface's variability and the large range of adsorption energies. Unlike other models that assume consistent changes in adsorption energy, the Jossens model is specifically intended for analyzing complex surfaces, making it particularly appropriate for materials like NH_2-Ag-MOF, which has a variety of active sites due to the attendance of amino and silver groups. The value of K at 15.38 in this situation indicates a significant attraction between Hg(II) ions and the NH_2-Ag-MOF surface, highlighting the adsorbent's capacity to efficiently trap mercury ions. This strong attraction is important in situations where effective and dependable removal of mercury from wastewater is needed. The value 0.022 for the parameter J represents the distribution of adsorption energies. A lower J indicates a narrower distribution, which suggests that most active sites on NH_2-Ag-MOF have similar energy levels. This uniformity suggests steady and consistent adsorption effectiveness over a variability of mercury concentrations, which is particularly advantageous in real-life situations where mercury levels can vary. By accounting for energy distribution, the Jossens model suggestions a thorough understanding of the dynamics of adsorption on heterogeneous surfaces. This understanding helps in enhancing the performance of NH_2-Ag-MOF under different operational conditions. In summary, the K and J parameters offer a thorough and accurate assessment of NH_2-Ag-MOF's ability to adsorb, its effectiveness, and its stability. This makes the Jossens model extremely valuable for improving applications aimed at removing mercury, especially in cases where surface heterogeneity plays a significant role in the adsorption technique.[61]

3.4. Kinetics of the adsorption

The Fig. S3(b) represented the influence of contact duration on the adsorption of Hg(II) ions onto NH_2-Ag-MOF, illustrating a swift initial uptake followed by a gradual stabilization toward equilibrium. In the initial phase, spanning the first few minutes, a pronounced increase in the adsorption rate is evident, which signifies the availability of numerous active adsorption sites, including amino-functional groups and Ag-coordination centers, for interaction with Hg(II) ions.[66] This phase is predominantly characterized by external surface adsorption and surface diffusion, facilitating the rapid binding of Hg(II) species to the adsorbent. As time advances, the adsorption curve begins to plateau, indicating a deceleration in uptake due to the increasing occupation of these active sites and the subsequent diffusion of Hg(II) ions into the internal pores of the framework. Following a duration of approximately 70–80 min, the adsorption process attains equilibrium, beyond which no significant additional increase in adsorption capacity is observed. This behavior suggests that the available sites have reached saturation, or that mass transfer limitations have been imposed. The ultimate recorded adsorption capacity exceeds 570 mg g^{-1}, evidencing the pronounced affinity of NH_2-Ag-MOF toward Hg(II) ions and underscoring the necessity of sufficient contact time to fully capitalize on the high-capacity structure of the adsorbent. This kinetic profile emphasizes that, although initial removal is rapid, the attainment of maximum adsorption necessitates ample exposure time to permit Hg(II) ions to diffuse deeper into the porous architecture of the MOF, thereby optimizing removal efficiency for practical applications in wastewater treatment.

It is highly advantageous to use adsorption kinetic models to investigate the adsorption and removal of Hg(II) from NH_2-Ag-MOF. These models provide an inclusive insight of the procedure's pace, mechanism, and overall efficacy. Researchers can assess the rate of absorption of Hg(II) ions and ascertain whether physisorption or chemisorption is the predominant mechanism by using pseudo-first-order,[67] pseudo-second-order,[68] and intraparticle diffusion models.[69] An approximate first-order model points to physical adsorption, while an approximate second-order model indicates chemisorption, suggesting stronger interactions with the NH_2-Ag-MOF amino

and silver groups. Predicting the stability and efficacy of adsorption more precisely is made possible by an understanding of the main mechanism.[70] The rate coefficients and equilibrium adsorption capabilities can be found using kinetic models, which offer important information on how quickly Hg(II) can be removed under different circumstances. This is an important consideration for efficient wastewater treatments.[70] By identifying whether adsorption is impacted by surface contacts, film diffusion, or internal particle diffusion, as well as identifying any potential processes that can restrict the rate of adsorption, the intraparticle diffusion model digs further into the process. The detailed understanding of how adsorption works helps to adjust how long the contact time is and how much adsorbent is used for the best results. Kinetic models that describe how adsorption happens can help when designing and improving NH_2-Ag-MOF for removing mercury from wastewater. This ensures that the treatment process is fast and effective, and can be used on a large scale (Table S5).

To illustrate how Hg(II) is adsorbed onto NH_2-Ag-MOF, the pseudo-first-order adsorption kinetic model is helpful. It helps to easily assess the original adsorption rate and efficiency by simplifying and focusing on the interaction mechanism driven by physical forces. According to this model, the difference among the equilibrium concentration and the quantity of Hg(II) adsorbed at a assumed time determines how quickly NH_2-Ag-MOF may absorb mercury ions. This aids in evaluating the adsorption rate of the substance.[67] The rate constant K_1, which was found to be 0.0915 $min^{-1} \times 10^{-2}$ in the current research, provides valuable data on the degree of adsorption. The time needed for NH_2-Ag-MOF to adsorb a significant amount of material can be estimated using this data. A smaller K_1 value suggests that the adsorption process may proceed consistently and gradually, potentially indicating a more lasting and stable bond over time, even if the initial uptake rate is slower.[69] For preliminary studies to ascertain the speed at which NH_2-Ag-MOF reacts to Hg(II), the pseudo-first-order model is useful. This is critical for applications requiring swift remediation. The simplicity of the model assistances in understanding how the adsorption process in NH_2-Ag-MOF may be governed by surface diffusion and physical adsorption forces, like van der Waals connections (Fig. 7(c and d)).[67] By employing the pseudo-first-order model, researchers can learn more around the adsorption kinetics of NH_2-Ag-MOF. If a more thorough comprehension of the underlying mechanisms is needed, this information can be further extended to more complex models and can be useful in enhancing the elimination of Hg(II) during the early stages of wastewater treatment (Table S7).

The procedure of Hg(II) adsorption on NH_2-Ag-MOF is fully clarified by the pseudo-second-order adsorption kinetic model.[68] This model focuses on the chemisorption mechanism, which involves electron involvement or valence forces among the active sites on the MOF's surface, like its silver and amino groups, and Hg(II) ions.[68] This particular model is well suited for materials in which adsorption is expected to result in strong, potentially covalent or complex bonds. This suggests that the binding of Hg(II) onto NH_2-Ag-MOF is not only fast but also long-lasting and secure. The rate constant K_2 of g mg^{-1} $min^{-1} \times 10^{-2}$ indicates a steady adsorption rate, resulting in a highly stable attachment of Hg(II) ions, although the process is gradual. The NH_2-Ag-MOF possesses a regulated rate of adsorption which allows it to maintain effectiveness over an extended period, making it a dependable choice for scenarios requiring ongoing removal of mercury. Exhibiting an equilibrium adsorption capacity q_e of 636.8 mg g^{-1}, this substance show cases its capability to trap a substantial quantity of mercury ions, illustrating the efficiency of the NH_2-Ag-MOF in adsorption. The high q_e indicates that the pseudo-second-order model, showing that the NH_2-Ag-MOF effectively holds onto mercury ions for an extended period, supports chemisorption. This characteristic makes it suitable for environments with high concentrations of mercury, such as industrial wastewater. The stability offered by chemisorption ensures that, even with fluctuations in mercury levels, the material remains effective and poses minimal risk of releasing the mercury. By concentrating on the kinetics of chemisorption, the pseudo-second-order model improves the ability to predict long-term performance and assists in optimizing operational parameters for the expansion of NH_2-Ag-MOF's use in practical applications. The K_2 and q_e parameters in the model yield significant data regarding the speed and volume of adsorption, key factors in developing reliable systems for removing mercury effectively. This model supports the extensive application of NH_2-Ag-MOF in industrial wastewater treatment, establishing a robust framework for consistently maintaining high mercury removal efficiency in diverse situations. The pseudo-second-order kinetic model is generally essential for comprehending, forecasting, and improving the adsorption characteristics of NH_2-Ag-MOF. It offers a solid basis for optimizing its effectiveness in environmentally friendly mercury removal procedures (Fig. 7(c and d)).

The model for intraparticle diffusion adsorption offers important analysis into how Hg(II) is adsorbed onto NH_2-Ag-MOF, highlighting the significance of mercury ion diffusion within the adsorbent particles in affecting the adsorption process.[69] This design is ideally suited for NH_2-Ag-MOF because of its porous structure and variety of active sites. It helps to elucidate the movement and interaction of mercury ions on both the external and internal surface areas of the material. The K_i intraparticle diffusion rate constant, recorded at 81.93 mg g^{-1} $min^{-1/2}$, demonstrates how fast mercury ions spread within particles. A higher K_i value implies effective internal diffusion, which is advantageous for applications requiring rapid adsorption rates. The value of 29.11 mg g^{-1} for the intercept X designates the attendance of the boundary layer result. A higher X value suggests that surface adsorption plays a significant role before mercury ions enter the internal pores of NH_2-Ag-MOF.[70] To maximize contact duration and make efficient use of both external and interior adsorption phases, it is essential to comprehend the thickness of the borderline layer and the influence of surface adsorption. The intraparticle diffusion model can distinguish between surface and internal diffusion stages, giving researchers important insights into potential diffusion constraints. This enables targeted improvements, like

altering contact time or particle size, to improve adsorption effectiveness. The K_i and X parameters of this model allow for a complete empathetic of the multi-stage adsorption procedure. This optimization enables NH_2-Ag-MOF too effectively and scalable remove mercury in wastewater treatment, by fully utilizing surface and intraparticle adsorption dynamics.

For the analysis of Hg(II) adsorption onto NH_2-Ag-MOF, the Elovich adsorption kinetic model is helpful. The complex chemisorption processes on various surfaces with variable adsorption energies are easier to fully comprehend thanks to it. NH_2-Ag-MOF contains various active sites such as amino and silver groups. These sites are believed to interact with Hg(II) ions through different binding mechanisms, and the Elovich model is able to effectively represent this range of interactions. The desorption rate constant β of the model, which was measured at 139.58 (g mg^{-1}), indicates very little desorption.[71] This suggests that once the Hg(II) ions are adsorbed, they stay firmly bound to NH_2-Ag-MOF. As a result, it is well suited for applications that require long-term mercury retention. This stability is especially helpful in the wastewater treatment industry, where constant and reliable mercury removal is crucial. The adsorption process begins slowly, allowing Hg(II) ions to enter the adsorbent structure more deeply, as seen by the first adsorption rate constant α of 0.01 (mg g^{-1} min^{-1}).[70] This results in the formation of strong and stable bonds, rather than just adhering to surface sites, making it critical for effective mercury removal. The gradual binding process is well-suited for processes dominated by chemisorption, enabling mercury ions to form more enduring bonds with the functional groups of NH_2-Ag-MOF over time. Using the parameters α and β, the Elovich model offers significant data about the long-term stability of Hg(II) adsorption as well as the initial adsorption kinetics.[72] Therefore, it serves as a valuable tool for enhancing contact time, adsorbent dosage, and process parameters. This model has demonstrated a high degree of efficacy in predicting NH_2-Ag-MOF performance in real-world mercury removal scenarios. It is crucial for sustainable, extensive wastewater treatment that the material remains stable and consistently efficient in adsorbing mercury.

3.5. Diffusion mechanism

Fig. 7(e) depicts the fitting outcome of the IPD model. The complete process involves three stages: (i) extensive pore diffusion, corresponding to speedy adsorption and a high K_{d1} value; (ii) the diffusion of microporous materials is in alignment with medium absorption and the K_{d2} value, (iii) equilibrium adsorption occurs when the rate of adsorption is slow and the K_{d3} value is minimal. According to the K_{di} values at each step, as the reaction proceeds, it can be inferred that the rate of adsorption falls, suggesting that the first two stages have the most influence on the adsorption behavior.

3.6. Adsorption thermodynamics

The Fig. S3(c) illustrates the impact of temperature on the efficiency of Hg(II) ion removal by NH_2-Ag-MOF, revealing a significant enhancement in adsorption performance as the temperature increases from 20 to 45 °C. At lower temperature conditions, the removal efficiency remains relatively low, attributable to the diminished mobility of Hg(II) ions and restricted interaction with available active adsorption sites. As the temperature escalates, a corresponding increase in removal efficiency is observed, suggesting that the adsorption process is fundamentally endothermic. Elevated temperatures contribute to an increase in the kinetic energy of Hg(II) ions, a reduction in the viscosity of the solution, and an augmentation of diffusion rates. These factors enable the ions to enter the porous framework of NH_2-Ag-MOF more readily and engage with the amino and silver coordination centers. This temperature-dependent improvement persists until reaching the maximum assessed temperature of 45 °C, where the removal efficiency approaches nearly 100%. The consistent rise in efficiency substantiates the notion that higher temperatures promote stronger binding interactions and expedite the adsorption mechanism, thereby enhancing the adsorbent's ability to remove Hg(II) from the solution. Collectively, these findings confirm that NH_2-Ag-MOF demonstrates exceptional adsorption characteristics under thermally activated conditions, rendering it particularly effective for mercury remediation in contexts where effluent temperatures may be inherently increased, such as in various industrial applications[73–75]

The capacity of materials to absorb heavy metals is meaningfully influenced by temperature. The behavior of NH_2-Ag-MOF in absorbing Hg(II) at three distinct temperatures 298, 308, and 318 K was examined. Table S5 displays the thermodynamic parameters, including standard enthalpy ($\Delta H°$), standard entropy ($\Delta S°$), and Gibbs free energy ($\Delta G°$), which were calculated (Table S5).[76] The adsorption procedure of Hg(II) onto NH_2-Ag-MOF is endothermic, as indicated by the positive value of $\Delta H°$ in Table S8 and Fig. 8(a, b).[77,78] The adsorbent surface and Hg(II) interface are more disordered, as indicated by the positive values of $\Delta S°$. As temperature increases, the $\Delta G°$ value decreases, leading to an increase in the spontaneity of the reaction. This suggests that higher temperatures promote the advancement of the reaction (Fig. 8(c)).[79,80] It may be concluded that the Hg(II) adsorption onto NH_2-Ag-MOF is classified as chemical adsorption when combined with the normal adsorption energy (E_a) of 35.1 kJ mol^{-1} and the Gibbs free energy $\Delta G°$. For Hg(II) adsorption, the NH_2-Ag-MOF generally exhibits a spontaneous endothermic reaction, as shown in Table S8.[81,82]

3.7. Reusability

The absorption procedure was started by treating 50 mL of a 200 mg per L Hg(II) solution with 0.02 g of NH_2-Ag-MOF for one hour at a pH of 4. Following filtering, the Hg(II)-loaded absorbent was covered with 50 mL of EDTA solution (0.05 mol L^{-1}), which was then agitated for 3 hours at 25 °C.[83,84] The NH_2-Ag-MOF was extracted from the combination by centrifugation, and the mixture was washed with bi-distilled water. After drying under vacuum at 70 °C, it was then used again in the following cycle. Adsorption and repetition were carried out five times. The strong reactivation ability of a sorbent is necessary for any possible commercial use.[34,85] When EDTA was utilized to assess the restoration of NH_2-Ag-

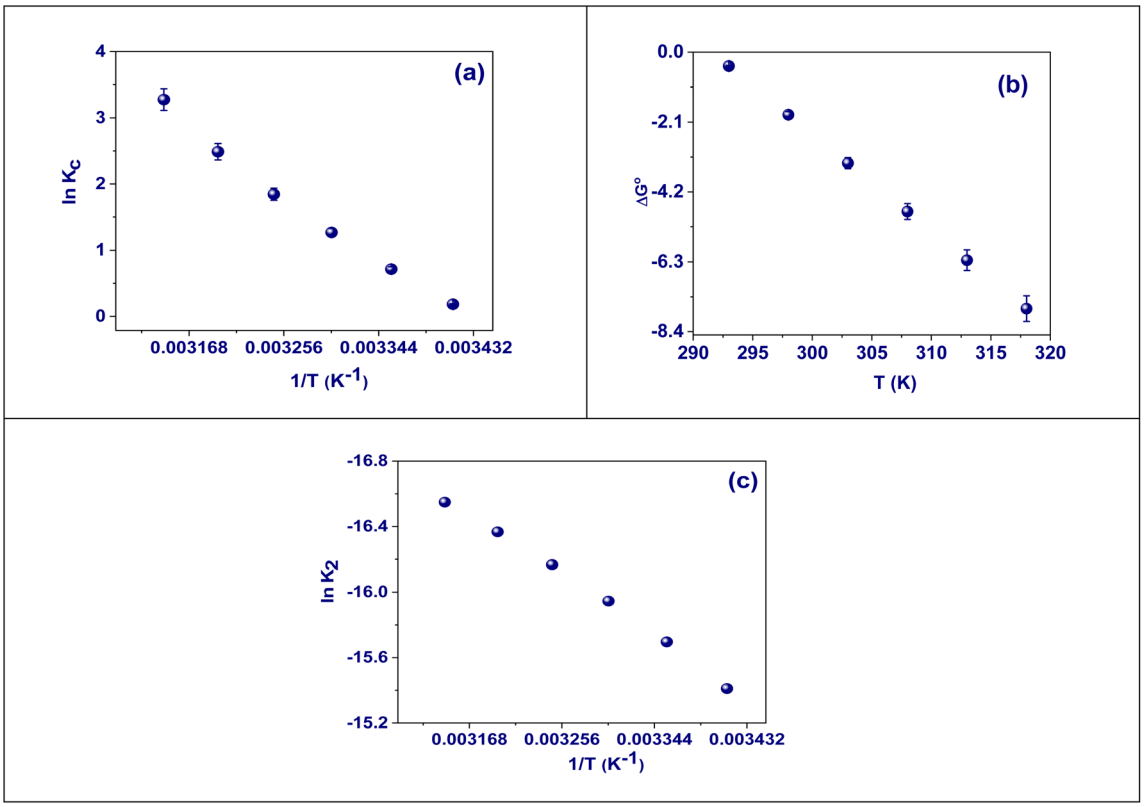

Fig. 8 (a) The Van't Hoff model of thermodynamic adsorption, (b) the temperature effect on free Gibb's energy, and (c) Arrhenius model.

MOF for removing Hg(II), it was found that 92% of the Hg(II) was escaping from the sponge. Over five series of sorption–desorption–sorption, the capabilities were 98.6, 97.2, 94.8, 90.6, and 84.2% of the original capacity, respectively (Fig. S4(a)). Perhaps as a result of the loss of vigorous sites and modifications to the specific geometric structure, the amount of uptake gradually reduced as the number of cycles rose. According to these findings, NH_2-Ag-MOF may be efficiently recycled.[13,19,86] The regenerated NH_2-Ag-MOF has an XRD pattern in Fig. S4(b) that shows very good structural stability for the adsorbent after the adsorption–desorption process. The peaks for diffraction from the regenerated material are still well defined and closely match those of pristine NH_2-Ag-MOF, meaning that the crystalline framework is mostly kept. There is no significant shifting or disappearing of peaks, nor any new peaks forming; this means there was no structural collapse and phase transformation during regeneration. A small decrease in peak intensity might be seen but can be due to little surface coverage or leftover adsorbate rather than degradation of the framework itself. The fact that characteristic diffraction features are retained proves that the coordination environment and long-range order of the MOF have stayed intact, which emphasizes its strength under operational conditions. Therefore, the results from XRD clearly indicate high regeneration capability and structural durability for NH_2-Ag-MOF; hence it could be considered a promising and reusable adsorbent for Hg(II) removal. The SEM image of regenerated NH_2-Ag-MOF in Fig. S4(c) indicates that the adsorbent retains its morphological integrity after the adsorption desorption process of Hg(II). From this micrograph, it is clear that material has an aggregated and layered structure with particle sizes still within nanoscale range (about 20 to 150 nm), which means there was no major structural collapse or fragmentation of particles during regeneration. The texture on the surface looks fairly rough and unbroken, indicating that most active sites as well as the porous framework have been preserved. There are no clear signs showing severe agglomeration, dissolution, or deformation; hence material's strong nature under these tested conditions is confirmed. Even if slight alterations in surface characteristics might be found, they could be due to adsorption and desorption interactions instead of lasting structural damage. In general terms, SEM analysis proves that NH_2-Ag-MOF has great morphological stability and reusability which backs up its claim to serve as a long-lasting adsorbent for repeated cycles of Hg(II) removal.

3.8. Frontier molecular orbitals and DFT calculations

Using the Gaussian16 software, density functional theory (DFT) simulations were performed to examine the interaction of glutamic acid and Hg(II). To understand a molecule's reactivity and look into the electron transfer among the highest occupied molecular orbital (HOMO) as well as the lowest unoccupied molecular orbital (LUMO), it is important to use a study of the border molecular orbitals. Fig. 9(a). A molecule's interaction with metals can be inferred from the difference in energy levels between its E_{HOMO} and E_{LUMO} (Fig. 9(b)). The band gap energy

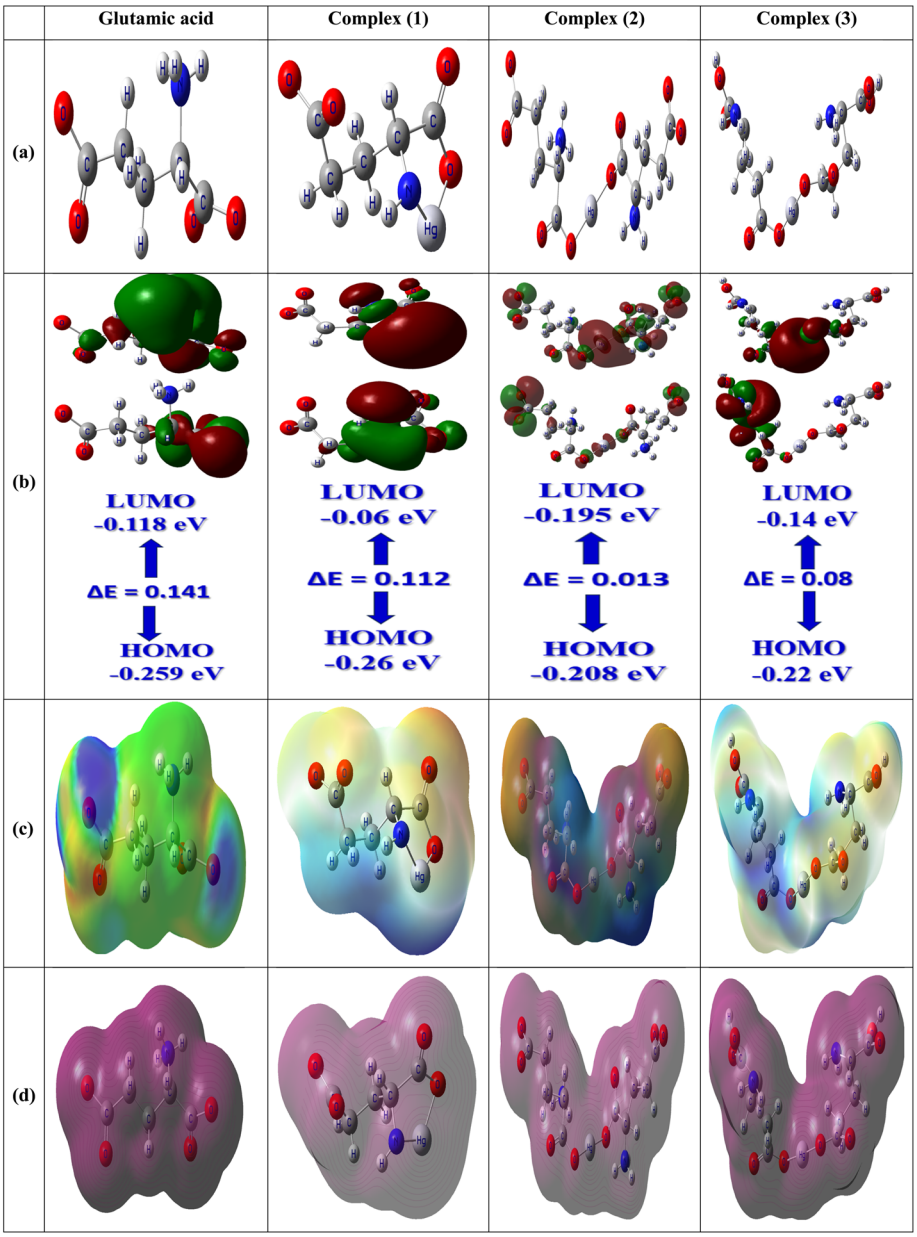

Fig. 9 (a) B3LYP/6-311G(d, p) level enhanced structure, (b) E_{HOMO} and E_{LUMO} energy levels, (c) electrostatic potential map (ESP), and (d) contour map of glutamic acid, complexes position (1), (2), and (3).

values for glutamic acid and its complexes at positions 1, 2, and 3 were determined to be 0.141, 0.112, 0.013, and 0.08 eV, respectively. This study suggests that the stability ranking is complex 1 < complex 2 < complex 3. The information is supported by the experimental data from the B–H plots, which show that the complexes' binding affinity values increase in the same order.[87,88] The electrostatic potential (ESP) map in Fig. 9(c) was used to measure the surface charge of glutamic acid molecules both before and after metal complexation. Divalent metal ions surround the negative charge, according to the results, indicating that the charges were moved from the ligand to the metal cations during the metal's complexation.[64]

Analyzing the electron distribution in glutamic acid and its bonding with mercury utilizing Gauss View software provides a thorough insight into the molecular arrangement, distribution of electric charge, and dynamics of interaction. This is essential for enhancing comprehension of the stability and reactivity of these compounds. Electron density maps offer in-depth insights into the bonding of atoms, allowing researchers to identify specific locations, such as carboxyl or amino groups, where mercury can bond. This is crucial for predicting the biological interactions and potential harmful effects of substances with accuracy. This analysis is helpful for evaluating how charges are distributed and for identifying polar regions and areas where electrons are either given or taken, all of which are important for understanding how mercury binding affects the function of glutamic acid. Gauss View allows for the visualization of molecular orbitals and potential electron

transfer by mapping electron density (Fig. 9(d)). This is useful for studying the effects of mercury on electron-rich systems. Additionally, insights into electron density can help researchers validate theoretical models used in predicting toxicity and reactivity in environmental and medicinal chemistry. This thorough method assists in identifying energy and stability influences, leading to the discovery of low-energy shapes and possible structural alterations caused by mercury. This is essential for the progression of research in areas such as environmental toxicology and pharmacology.

The importance of contour plots in the examination of glutamic acid and its mercury complexes cannot be overstated in the realm of molecular chemistry. These visualizations provide an in-depth and detailed depiction of electron density distribution, offering valuable insights into molecular interactions and stability. Contour plots are useful for identifying areas with different electron density, this is essential for identifying possible binding sites and comprehending the interactions between mercury and functional groups such as glutamic acid's carboxyl or amino groups. The diagrams illustrate small fluctuations in electron density that arise when mercury forms complexes. This allows researchers to identify alterations that reveal the reactivity, stability, and impact on the biochemical role of glutamic acid within these complexes.[57] Additionally, contour graphs simplify the visualization of alterations in molecular orbitals, providing a better understanding of electron transfer capacity and bonding properties. This detailed information helps make predictions about how toxic mercury–glutamic acid complexes will behave in the environment. Contour analysis is a highly valuable tool in computational chemistry, environmental science, and pharmacology for understanding the impacts of heavy metal interactions with biomolecules (Fig. 9(d)).

3.9. Interaction mechanism

There are four ways that the NH_2-Ag-MOF can adsorb mercury: surface complexation, cation exchange, pore filling, and electrostatic communication. The main mechanism for mercury adsorption on the adsorbents was chemical adsorption, according to the findings of kinetics and isotherm tests. Nevertheless, the NH_2-Ag-MOF's high surface area and variety of porous materials can also cause van der Waals forces to cause physical adsorption, as well as pore filling. Adsorbent material offers potential for removing mercury from contaminated water and industrial effluents. This is due to its ability to adsorb mercury through multiple pore sizes, as indicated by the intraparticle diffusion model. Hg^{2+} is the most prevalent species at a pH level of less than 2, whereas $Hg(OH)_2$ is leading at a pH level higher than 4. Both species and $Hg(OH)^+$ can coexist in aqueous solutions with pH values between 2 and 4. The negatively charged surface of the NH_2-Ag-MOF composites attracts Hg^{2+} and $Hg(OH)^+$ *via* electrostatic contact when the pH is 4. A variety of surface useful groups, such as COO^-, and O^-, can interact with the cation's ions. On the other hand, $Hg(OH)_2$ do not carry a charge, showing that electrostatic interaction does not impact the adsorbent surfaces when the pH is above 4. Still, the NH_2-Ag-MOF demonstrates a significant 96.5% removal efficiency at a pH of 4. NH_2-Ag-MOF effectively removes mercury ions from water solutions thanks to a variety of adsorption processes.[33,35] The molecular-level binding of the adsorption places to the target contaminants has been confirmed by the DFT calculations. Fig. 10 shows the improved surface electrostatic potential distribution and structures. The color bar's blue-to-red gradient represents a slow increase in electrostatic potential from negative to positive. The distribution of electrostatic potential in both states indicates that the various nitrogen functional groups are where the majority of the negative potential is located. Compared to the reduction state, the lowest oxidation state is lower. Nonetheless, mercury adsorption is more supported by negative electrostatic potential sites.[89]

3.10. Impact on actual water samples

The NH_2-Ag-MOF was tested to see how it could be used to treat actual wastewater from a coating ability. The effluent sample

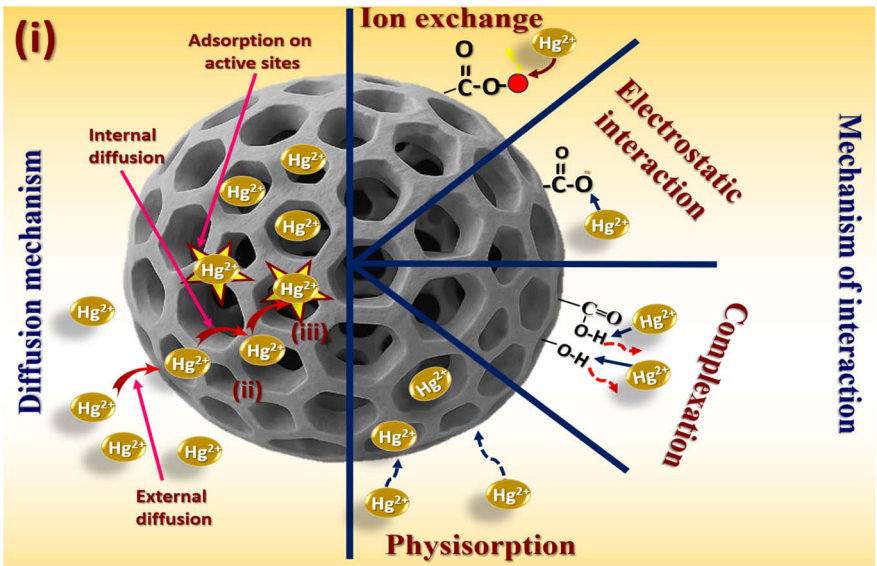

Fig. 10 Schematic diagram of mechanism of interaction.

Table 2 Different adsorbents' Hg(II) adsorption capacities

Adsorbents	BET ($m^2\ g^{-1}$)	T (°C)	pH	Q_e (mg g^{-1})	References
PAC	1786.9	25	7	405	90
SBA-15	148.7	25	6	40.4	91
Zeolite	126.9	25	6	84.24	92
PAAM-NH_2-MCM-41	646	25	5.2	177	93
Chitosan/MCM-41-PAA	253.31	25	4	164	94
$NiFe_2O_4$-PAC-SH	1700.4	25	7	298.8	90
$CoFe_2O_4$@mSiO_2-NH_2	147.08	25	7	149.3	95
Ppy-SBA-15	49.6	48	8	200	96
APTMs-modified TO-NFC	129.32	50	3–7	242.1	97
Starch/SnO_2	78.5	25	7	192	98
NH_2-Ag-MOF	1750.49	25	4	635.7	This search

was taken from a manufacturing area. The electroplating wastewater has high levels of heavy metal ions including Cr(VI) (9.42 mg L^{-1}), Cd(II) (11.86 mg L^{-1}), Ni(II) (14.62 mg L^{-1}), Cu(II) (7.88 mg L^{-1}), Zn(II) (6.84 mg L^{-1}) and Hg(II) (8.44 mg L^{-1}). The specified concentration used was 0.08 g L^{-1}. According to Fig. S5, the NH_2-Ag-MOF has a removal efficiency of 98.6% for Hg(II) and the content of Hg(II) after treatment is lower 0.1 mg L^{-1}, assembly the principles of the "Emission Standard of Pollutants for Electroplating". This indicates that the NH_2-Ag-MOF is a very promising adsorbent having a very discerning adsorption for Hg(II) in applied use.[83,84]

Table 3 Details regarding the Hg(II) adsorption capability and response surface of the central compound design

	Actual variables			Adsorption capacity (mg g^{-1})		
Run	Dose (g)	Time (min)	pH	Experimental	Predicted	Residue
1	10.4	5	7	33.88	4.85	29.03
2	10.4	100	7	438.41	470.57	−32.16
3	0.8	52.5	1	360.86	364.03	−3.17
4	10.4	52.5	4	444.13	444.13	0.0000
5	10.4	100	1	329.38	358.40	−29.03
6	0.8	52.5	7	461.90	461.94	−0.0442
7	0.8	100	4	635.70	603.50	32.20
8	10.4	52.5	4	444.13	444.13	0.0000
9	10.4	5	1	25.45	−6.70	32.16
10	10.4	52.5	4	444.13	444.13	0.0000
11	20	5	4	30.70	62.90	−32.20
12	10.4	52.5	4	444.13	444.13	0.0000
13	20	52.5	7	303.88	300.70	3.17
14	10.4	52.5	4	444.13	444.13	0.0000
15	20	52.5	1	274.94	274.89	0.0443
16	20	100	4	397.31	368.33	28.98
17	0.8	5	4	49.12	78.10	−28.98

3.11. In contrast to other adsorbents

A comparison between the synthesized NH_2-Ag-MOF and other adsorbents found in the literature was conducted. The synthesized NH_2-Ag-MOF has a higher adsorption capability than many other compounds (Table 2).

3.12. Analyzing response surfaces and modeling experimental designs

3.12.1. Investigative statistics. The suitability of the adsorption system design model and the adsorbate molecules' capacity to stay on the adsorbent superficial are what determine the adsorption procedure's effectiveness in commercial applications. Optimizing the adsorption capability (Y) with the Box–Behnken design, as indicated in Table 3, is crucial to achieving this. For several reasons, the two-factor interaction model was suggested as a way to navigate the design space. One explanation is that the experimental design configuration makes it impossible to estimate some main effects or interactions between variables independently, which is known as aliasing of the cubic model. Because of this, it could be difficult to correctly interpret the findings and discern the actual impacts of the variables.[31] Next, the quadratic model has R^2, adjusted R^2, and predicted R^2 values around 0.9862, 0.9685, and 0.7793, individually. A_{deq} precision evaluates the signal to noise ratio, with a ratio above 4 being preferable. The adequate signal is designated by the ratio of 24.263. Furthermore, the quadratic interaction and linear two-factor models also exhibit statistical significance, with sequence probability values of around 0.0010, 0.782, and >0.0001. Furthermore, as Table 4 illustrates, this is the highest-order polynomial wherever the extra terms have meaning and the classic is not aliased.

Table 4 Sequential model sum of squares

Source	Sum of squares	d_f	Mean square	Sequential p-value	Adjusted R^2	Predicted R^2	
Linear	1.616×10^5	9	17 952.58	0.0010	0.6356	0.5011	
2FI	1.456×10^5	6	24 274.47	0.7802	0.5730	0.1311	
Quadratic	7526.79	3	2508.93	<0.0001	0.9685	0.7793	Suggested
Cubic	0.0000	4			1.0000		Aliased

Table 5 Evaluating the variance of the models that have been fitted

Source	Sum of squares	D_f	Mean squares	F-value	P-value	
Model	5.382×10^5	9	59 797.74	55.61	<0.0001	significant
A-pH	7653.44	1	7653.44	7.12	0.0321	
B-dose	31 343.07	1	31 343.07	29.15	0.0010	
C-time	3.451×10^5	1	3.451×10^5	320.98	<0.0001	
AB	1299.57	1	1299.57	1.21	0.3080	
AC	2530.64	1	2530.64	2.35	0.1689	
BC	12 096.15	1	12 096.15	11.25	0.0122	
A^2	28 716.02	1	28 716.02	26.71	0.0013	
B^2	523.94	1	523.94	0.4873	0.5077	
C^2	1.009×10^5	1	1.009×10^5	93.80	<0.0001	
Residual	7526.79	7	1075.26			
Lack of fit	7526.79	3	2508.93			
Pure error	0.0000	4	0.0000			
Cor. total	5.457×10^5	16				

3.12.2. ANOVA analysis. The ANOVA investigation was utilized to determine the fit and importance of the interaction between two factors in Table 5. With a Fisher value of 55.61, the model is reflected statistically important. A Fisher value this high suggests that it is unlikely to occur due to random chance in less than 0.01% of cases, indicating that it may be due to other factors. Each term's significance was determined by probability values less than 0.05. A Fisher lack-of-fit value of 7526.79 suggested that the absence of fit was important. There is a 0.01% accidental that a high Fisher lack-of-fit rating is the result of random variation.[99]

For varying factor values, the reaction can be predicted using the equation with coded factors. High-level variables are automatically entered as +1, whereas low-level factors are designated as −1. When comparing component coefficients and assessing their respective importance, this coded equation is useful. The coefficients for comparison are given by eqn (5):

$$q_e = 444.131 + 30.9302 \times A + -62.593 \times B + 207.707 \times C - 18.0247 \times AB + 25.1528 \times AC - 54.9912 \times BC - 82.5836 \times A^2 - 11.1551 \times B^2 - 154.767 \times C^2 \quad (5)$$

The equation based on real factors can be used to predict the outcome levels of each ingredient.[75] In this case, the levels of each element should be stated clearly in their original units. Because the intercept is not at the exact center of the design space and its coefficients are changed to match the units of each factor, it should be highlighted that this equation is not appropriate to calculate the relative importance of each element (eqn (6)).

$$q_e = -162.656 + 80.9599 \times \mathrm{pH} + 4.83221 \times \mathrm{dose} + 12.1234 \times \mathrm{time} - 0.625859 \times \mathrm{pH} \times \mathrm{dose} + 0.176511 \times \mathrm{pH} \times \mathrm{time} - 0.120595 \times \mathrm{dose} \times \mathrm{time} - 9.17596 \times \mathrm{pH}^2 - 0.121041 \times \mathrm{dose}^2 - 0.0685948 \times \mathrm{time}^2 \quad (6)$$

The graphical representation shown in Fig. 11 is an effective method for confirming the accuracy of a regression model by supplying valuable data.[30,100] According to the first chart, which shows the standard probability in relation to externally studentized remains, the model structure and ANOVA effects are suitable (Fig. 11(a)). The accuracy of the linear trend (Fig. 11(b)) is confirmed by the second chart, the prediction against reality graph, which shows that the actual investigational effects match up smoothly with the expected values. Fig. 11(c) displays the Box–Cox plot, which is utilized to determine the most suitable power transformation for normalizing data. The vertical axis is labeled as Ln (Residuals) and represents the natural logarithm of the residual sum of squares. Lower values on this axis indicate more effective transformations that minimize residual error. The Lambda (λ) labeled horizontal axis displays different power transformations, with $\lambda = 1$ representing no transformation, $\lambda = 0$ indicating a log transformation, and other values representing varying levels of transformation. The green vertical line indicates the ideal lambda value, which is close to zero. This suggests that a log transformation with a lambda value around zero would be the most effective approach for reducing variance and promoting normal distribution in the data. The blue and red lines surrounding the optimal lambda, which means that any λ within this range would result in similar improvements in normality and residual minimization, indicate the confidence interval. This plot suggests that using a log transformation with a λ close to zero can assist in meeting statistical assumptions, ultimately improving data analysis by making the distribution of data more normal and homoscedastic.[101] The graph in Fig. 11(d) shows how the studentized external residuals are spread out based on the predicted responses. This helps to identify any outliers and evaluate how well the regression model fits. The plot shows that all of the student's external residues fall within the forecast boundaries and are uniformly distributed around 0.[102] The perturbation map in Fig. 11(e) displays the contrast of each variable at a specific place inside the carefully measured interplanetary design. To control the yield response, only one element was altered across its range; all other components remained unchanged. The story highlights how each component touches a particular region of the design setting (*e.g.*, pH, dosage, and time). It seems that each factor contributes to the adsorption capacity.[84] The correlation among

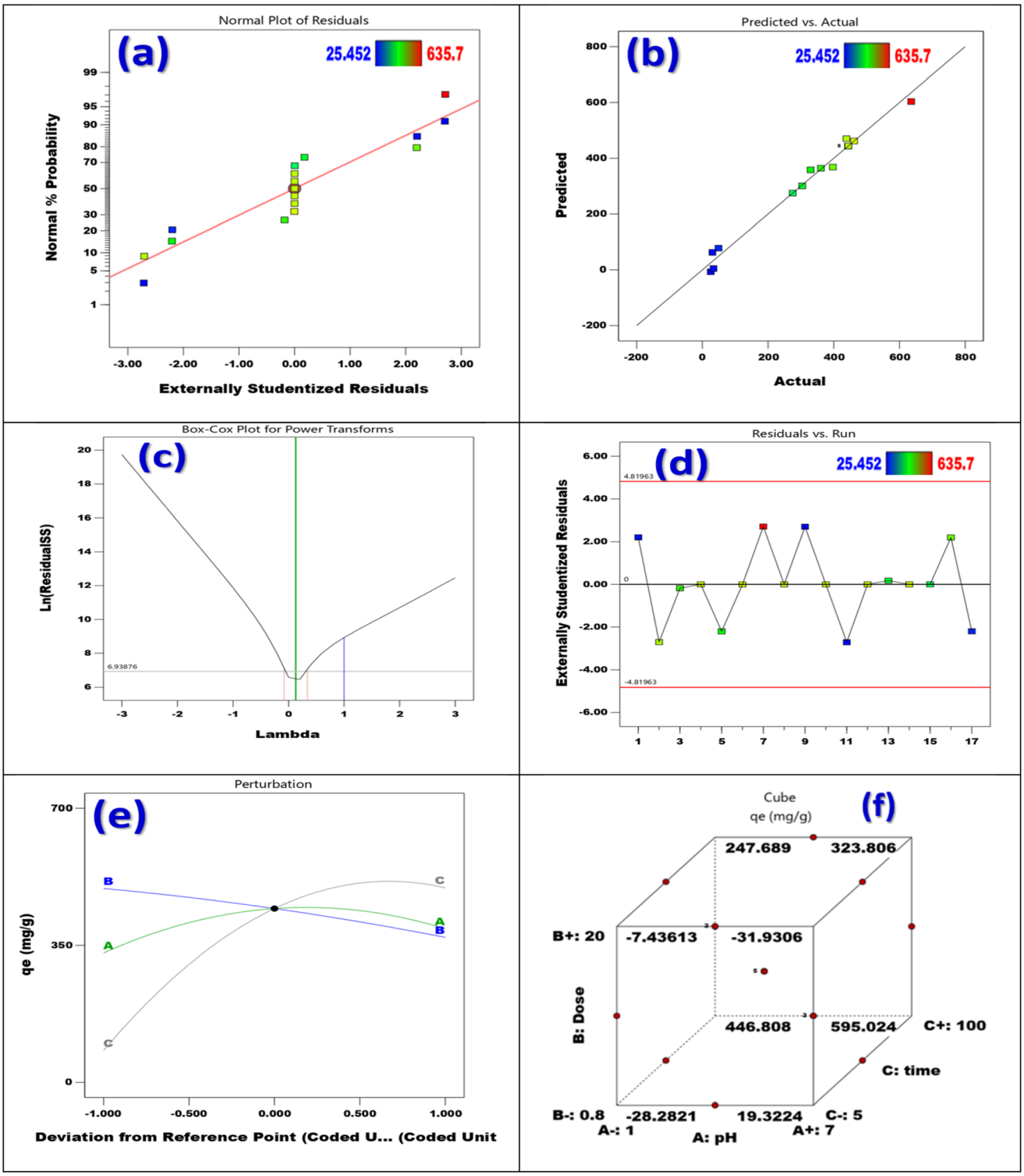

Fig. 11 (a) Plots of normal probability for residuals, (b) plots demonstrating the relationship among the expected and experimental values, (c) Box–Cox shows how the residuals change in relation to the lambda, (d) use a highly standardized residuals *vs.* residuals calculation, (e) plot the rate of response perturbation (for *A*: pH, *B*: dose, and *C*: time), and (f) graphical optimization of adsorption capacity.

pH and adsorption time demonstrated how quickly these variables affected adsorption capability. Determined which parameter had the greatest influence by looking at the factors in eqn (6). It was discovered that time, pH, and the adsorption dosage all consistently positively compressed the measured adsorption capability. The 3D cube plot shown in Fig. 11(f) demonstrates how three different variables pH (*A*), dose (*B*), and time (*C*) – affects a response variable, q_e in mg g^{-1}. Each axis

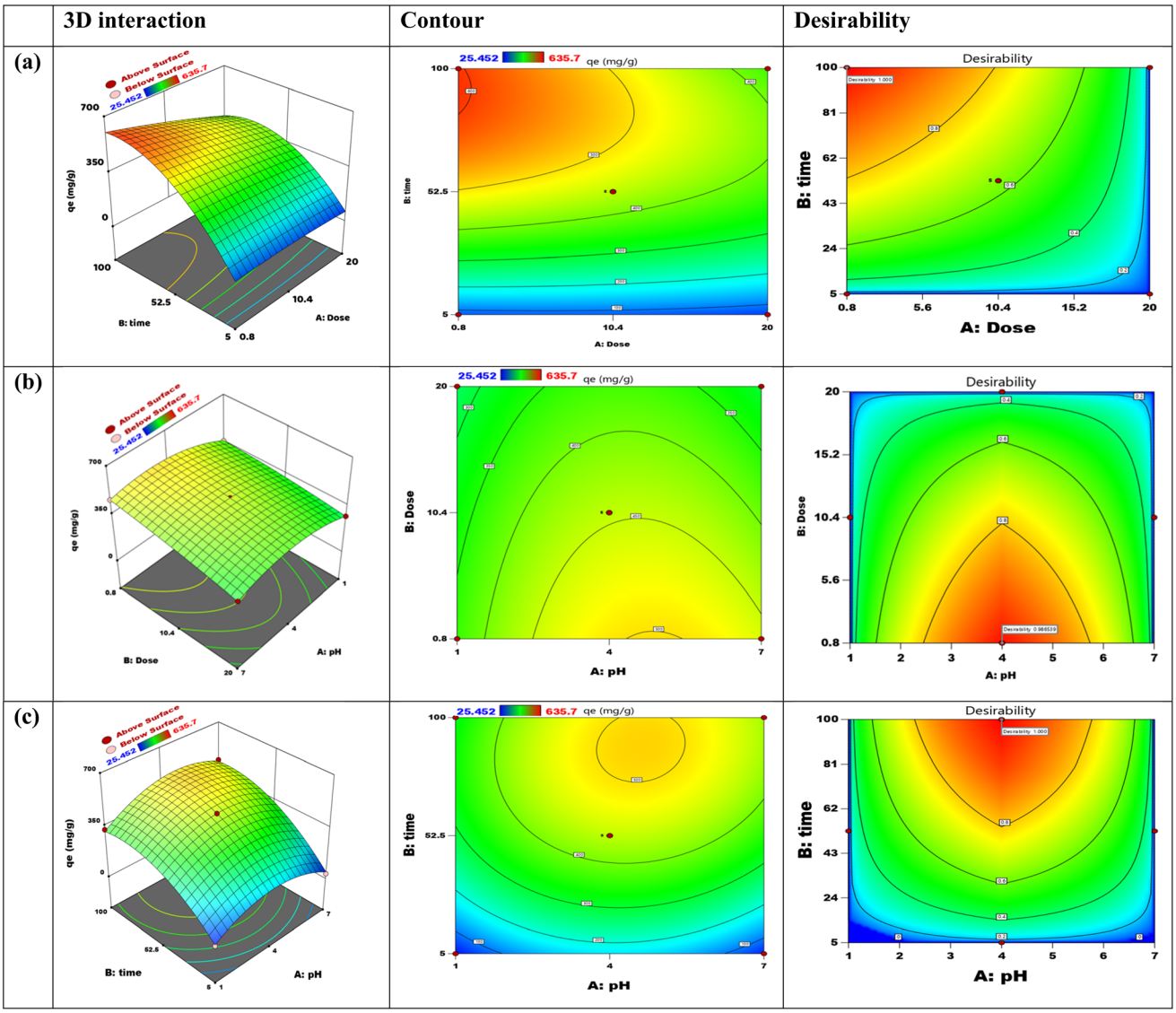

Fig. 12 3D interaction, contour, and desirability: (a) communication among dose and time, (b) dose and pH, and (c) interaction between pH and time.

represents one of the variables at two levels: pH ranges from 1 to 7, dose ranges from 0.8 to 20, and time ranges from 5 to 100. The numbers at the corners show q_e under various combinations of these factors, demonstrating how they interact. For instance, high q_e values (*e.g.* 595.024) indicate favorable conditions. This graphic provides a clear view of how pH, dose, and time affect q_e, identifying the best conditions and allowing for easy comparison to determine optimal factor settings for increasing or changing the response. It is a useful device for examining complicated interactions in investigational design.[103]

3.12.3. Adsorption capacity and the impact and adjustment of the input factors. 2D contour as well as 3D response surface plots, which illustrate how two different factors impact the response within the tested ranges while maintaining all other variables constant, are shown in Fig. 12(a–c) to help visualize how several factors interact and effect q_e. The relationship between the adsorption capacity (mg g^{-1}), the amount of adsorbent (g), the pH level, and the duration of contact (min) is shown in three dimensions in Fig. 12(a–c).[27,28] The findings indicate that the adsorption capacity can be increased by either extending the contact time or lowering the dosage of the adsorbent. Furthermore, it has been determined that the optimal pH for adsorption is 4, as this is where maximal capacity occurs. The desirability operation, which ranges from 0 to 1, is used for optimization. An answer with a value of 0 is seen as substantially different from the desired result, whereas a response with a value of 1 is regarded as desirable.[99,104]

3.12.4. Validating models and using the desirability method. Fig. 13(a) displays the optimal predicted values for the experimental settings to achieve the best performance (adsorption capability). The results of the desirability function are shown in Fig. 13(b). Within certain bounds, such as C_0 ranging from 100 to 800 mg L^{-1}, temperature from 20 to 45 °C,

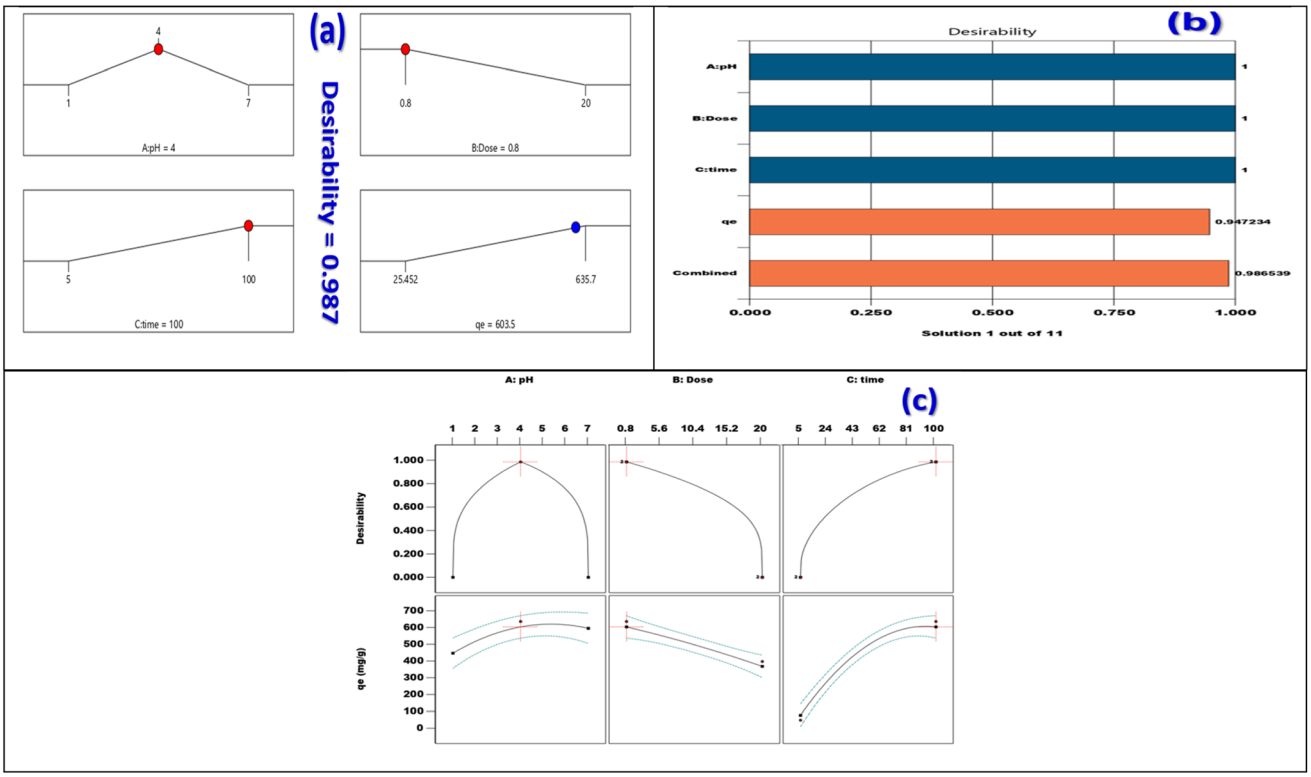

Fig. 13 (a) Increasing curiosity about the numerically optimal solutions, (b) each response's desirability, and (c) a bar graph representing individual desirability.

and contact time from 5 to 100 min, the experiment examined the response for each factor. The experiment's outcomes closely matched the anticipated reactions.[28] After that, two compliance tests were conducted using the adjusted input settings (Fig. 13(c)).[29,105] This experiment demonstrated the precision and efficacy of the BBD when combined with the want function to identify the optimal adsorption configuration for optimal output. Thus, under these favorable circumstances, further research on isotherms, kinetics, and thermodynamics was conducted.[99,103]

4. Conclusion

Because of the increasing amount of mercury pollution in industrial wastewater, many researchers have been working to find ways to get rid of Hg(II). However, the methods used to remove Hg(II) ions often end up removing other important metals as well, causing economic losses. In this research, a functionalized NH_2-Ag-MOF has been created to remove Hg(II) from solutions. This is achieved by incorporating glutamic acid to enhance the functional group on the adsorbent (NH_2-Ag-MOF). The absorbent was successfully created and examined using multiple approaches with XRD, FT-IR, XPS, SEM, EDX, and N_2 adsorption/desorption isotherm. These tests revealed a large surface area of 1750.49 $m^2\ g^{-1}$, a mesoporous pore size of 3.84 nm, as well as a pore volume of 3.38 $cm^3\ g^{-1}$. In addition, the study included batch experiments to examine the properties of absorbent amount, Hg(II) concentration, temperature, and time. The kinetic model was fitted to the pseudo-second-order, and the Langmuir equation was used to predict the adsorption isotherm. The adsorption energy of 31.6 kJ mol^{-1} demonstrated that the adsorption procedure type that was observed was chemisorption. The research found that the adsorption is endothermic, with a positive enthalpy ΔH° of 84.9 kJ mol^{-1} K^{-1}. Similarly, the entropy ΔS° is positively charged at 291.4 J mol^{-1} K^{-1}, showing that as temperature rises, randomness and removal also increase. The free Gibbs energy ΔG° becomes more negative with increased temperature, favoring both the adsorption and elimination of Hg(II). An analysis of the interaction between Hg(II) and NH_2-Ag-MOF has exposed that the adsorption procedure is significantly affected by the electrostatic interaction, according to density functional theory (DFT) controls. The material used to absorb the particles was discovered to be very reusable, showing effective performance. Response Surface Methodology (RSM) as well as Box–Behnken design (BBD) were employed to improve the absorption process' efficiency.

Author contributions

Ahlem Guesmi: conceptualization, data curation, investigation, validation, visualization, writing – review and editing. Faisal K. Algethami: methodology, writing – review and editing. Naoufel Ben Hamadi: conceptualization, data curation, investigation, visualization, writing – review and editing. Wesam Abd El-Fattah: conceptualization, data curation, investigation,

validation, writing – review and editing. Mohamed G. El-Desouky: conceptualization, data curation, investigation, methodology, software, writing – original draft. Ashraf A. El-Bindary: conceptualization, data curation, investigation, resources, validation, visualization, writing – review and editing.

Conflicts of interest

There are no conflicts of interest to declare.

Data availability

The data that support the findings of this study are available from the corresponding author upon reasonable request.

Supplementary information (SI) is available. See DOI: https://doi.org/10.1039/d6ra02574a.

Acknowledgements

This work was supported and funded by the Deanship of Scientific Research at Imam Mohammad Ibn Saud Islamic University (IMSIU) (grant number IMSIU-DDRSP2603).

References

1 M. Fayazi, Removal of mercury (II) from wastewater using a new and effective composite: sulfur-coated magnetic carbon nanotubes, *Environ. Sci. Pollut. Res.*, 2020, **27**, 12270–12279.

2 S. Abd El Wanees, M. G. A. Saleh, M. A. Hegazy, M. I. Alahmdi, K. A. Soliman, N. H. Elsayed, M. Abdelfattah, M. M. Aljohani, S. Nooh, M. Asab and S. S. Elyan, Mitigation of hydrogen production on C-steel in HCl solution using a benzylidene compound, *J. Adhes. Sci. Technol.*, 2024, **38**, 1161–1190.

3 A. A. Keshk, N. H. Elsayed, M. M. Zareh, D. A. K. Alenazi, S. Said, A. O. Alatawi, R. K. Albalawi, M. Maher, S. M. Algabry and K. Shoueir, Kappa-carrageenan for benign preparation of CdSeNPs enhancing the electrochemical measurement of AC symmetric supercapacitor device based on neutral aqueous electrolyte, *Int. J. Biol. Macromol.*, 2023, **234**, 123620.

4 A. A. Keshk, N. H. Elsayed, F. M. Almutairi, M. Al-Anazi, S. Said, H. M. Althurwi, R. K. Albalawi and M. R. El-Aassar, Effect of green and sustainable extracted fucoidan polysaccharide as a corrosion inhibitor in 3.5% NaCl, *Biomass Convers. Biorefinery*, 2023, 28219–28232.

5 X. Gao, H. Yin, C. Guo, B. Yan, M. Li, L. Xin and Z. Wu, Comprehensive removal of various dyes by thiourea modified chitosan/nano ZnS composite via enhanced photocatalysis: Performance and mechanism, *Int. J. Biol. Macromol.*, 2023, **247**, 125677.

6 F. M. Almutairi, Novel algae-chitosan/alginate beads for efficient basic Fuchsin removal: synthesis, characterization, adsorption study, mechanism, and optimization, *Int. J. Biol. Macromol.*, 2024, **280**, 135604.

7 N. N. Abd Malek, A. H. Jawad, K. Ismail, R. Razuan and Z. A. ALOthman, Fly ash modified magnetic chitosan-polyvinyl alcohol blend for reactive orange 16 dye removal: Adsorption parametric optimization, *Int. J. Biol. Macromol.*, 2021, **189**, 464–476.

8 L. A. Arni, A. Hapiz, A. H. Jawad, A. S. Abdulhameed, Z. A. ALOthman and L. D. Wilson, Fabrication of magnetic chitosan-grafted salicylaldehyde/nanoclay for removal of azo dye: BBD optimization, characterization, and mechanistic study, *Int. J. Biol. Macromol.*, 2023, **248**, 125943.

9 A. H. Jawad, U. K. Sahu, N. A. Jani, Z. A. ALOthman and L. D. Wilson, Magnetic crosslinked chitosan-tripolyphosphate/MgO/Fe_3O_4 nanocomposite for reactive blue 19 dye removal: Optimization using desirability function approach, *Surf. Interfaces*, 2022, **28**, 101698.

10 A. S. Abdulhameed, R. Wu, S. A. Musa, H. M. Agha, Z. A. ALOthman, A. H. Jawad and S. Algburi, Bisphenol-A-diglycidyl ether modified chitosan/nano-SiO_2 via hydrothermal process: A statistical modeling and adsorption mechanism for reactive orange 16 dye removal, *Int. J. Biol. Macromol.*, 2024, **256**, 128267.

11 A. S. Abdulhameed, A. Hapiz, S. A. Musa, Z. A. ALOthman, L. D. Wilson and A. H. Jawad, Biomagnetic chitosan-ethylene glycol diglycidyl ether/organo-nanoclay nanocomposite for azo dye removal: A statistical modeling by response surface methodology, *Int. J. Biol. Macromol.*, 2024, **255**, 128075.

12 M. Yanat and K. Schroën, Preparation methods and applications of chitosan nanoparticles; with an outlook toward reinforcement of biodegradable packaging, *Reactive Funct. Polym.*, 2021, **161**, 104849.

13 B. Hassan, V. K. Rajan, V. A. Mujeeb and K. Muraleedharan, A DFT based analysis of adsorption of Hg^{2+} ion on chitosan monomer and its citralidene and salicylidene derivatives: prior to the removal of Hg toxicity, *Int. J. Biol. Macromol.*, 2017, **99**, 549–554.

14 H. Sun, Y. Li, X. Chen, X. Chen, S. Li, W. Ma and K. Fu, Hypophosphorous acid functionalized nanoporous silicon for selective adsorption of Hg(II) in industrial waste water, *Chem. Eng. Res. Des.*, 2023, **197**, 264–273.

15 Y. Wang, S. Li, X. Wu, J. Zhang, J. Feng, M. Li, S. Zong and W. Yan, Nitrogen-Based conjugated microporous polymers for efficient Hg(II) removal from Water: Performance and mechanism, *Chem. Eng. J.*, 2023, **471**, 144659.

16 L. Cui, Y. Wang, L. Gao, L. Hu, L. Yan, Q. Wei and B. Du, EDTA functionalized magnetic graphene oxide for removal of Pb(II), Hg(II) and Cu(II) in water treatment: adsorption mechanism and separation property, *Chem. Eng. J.*, 2015, **281**, 1–10.

17 S.-H. Yoo, S.-C. Lee, M. Ko, S. Yoon, J. Lee, J.-A. Park and S.-B. Kim, Adsorption of Hg (II) on polyethyleneimine-functionalized carboxymethylcellulose beads: Characterization, toxicity tests, and adsorption experiments, *Int. J. Biol. Macromol.*, 2023, **241**, 124516.

18 K. Wu, B. Wang, T. Liu, J. Wang, W. Xu, B. Zhang and Y. Niu, Synthesis of salicylaldehyde tailored PAMAM

dendrimers/chitosan for adsorption of aqueous Hg(II): Performance and mechanism, *Int. J. Biol. Macromol.*, 2023, **253**, 126590.

19 J.-H. Jang, J.-D. Seo, S.-M. Paek and M. Park, Sulfide-occluded zeolites: Cooperative adsorption-precipitation system for near perfect decontamination of aqueous Hg species, *J. Environ. Chem. Eng.*, 2023, **11**, 110783.

20 B. Zeng, W. Wang, S. He, G. Lin, W. Du, J. Chang and Z. Ding, Facile synthesis of zinc-based organic framework for aqueous Hg(II) removal: Adsorption performance and mechanism, *Nano Mater. Sci.*, 2021, **3**, 429–439.

21 S. Ghosh, A. Othmani, A. Malloum, O. K. Christ, H. Onyeaka, S. S. AlKafaas, N. D. Nnaji, C. Bornman, Z. T. Al-Sharify and S. Ahmadi, Removal of mercury from industrial effluents by adsorption and advanced oxidation processes: A comprehensive review, *J. Mol. Liq.*, 2022, 120491.

22 Y. Xue, X. Fang, H. Jiang, J. Wu, H. Liu, X. Li, P. He, F. Li, Y. Qi and Q. Gao, Hierarchical microsphere Flower-like SnIn4S8 with active sulfur sites for adsorption and removal of mercury from coal-fired flue gas, *Chem. Eng. J.*, 2023, **472**, 145105.

23 X. Yan and H. Ge, Preparation of metal organic frameworks modified chitosan composite with high capacity for Hg(II) adsorption, *Int. J. Biol. Macromol.*, 2023, **232**, 123329.

24 A. S. Abdulhameed, N. N. M. F. Hum, S. Rangabhashiyam, A. H. Jawad, L. D. Wilson, Z. M. Yaseen, A. A. Al-Kahtani and Z. A. ALOthman, Statistical modeling and mechanistic pathway for methylene blue dye removal by high surface area and mesoporous grass-based activated carbon using K_2CO_3 activator, *J. Environ. Chem. Eng.*, 2021, **9**, 105530.

25 A. S. Abdulhameed, A. Mohammad and A. H. Jawad, Modeling and mechanism of reactive orange 16 dye adsorption by chitosan-glyoxal/TiO_2 nanocomposite: application of response surface methodology, *Desalination Water Treat.*, 2019, **164**, 346–360.

26 A. H. Jawad, M. M. Ishak, A. M. Farhan and K. Ismail, Response surface methodology approach for optimization of color removal and COD reduction of methylene blue using microwave-induced NaOH activated carbon from biomass waste, *Water Treat.*, 2017, **62**, 208–220.

27 R. T. Mogharbel, K. Alkhamis, R. Felaly, M. G. El-Desouky, A. A. El-Bindary, N. M. El-Metwaly and M. A. El-Bindary, Superior adsorption and removal of industrial dye from aqueous solution via magnetic silver metal-organic framework nanocomposite, *Environ. Technol.*, 2024, **45**, 2558–2574.

28 W. A. El-Fattah, A. Guesmi, N. B. Hamadi, A. Houas, M. T. Alotaibi, M. G. El-Desouky and A. Shahat, Novel composite from chitosan and a metal-organic framework for removal of tartrazine dye from aqueous solutions; adsorption isotherm, kinetic, and optimization using Box-Benkhen design, *Int. J. Biol. Macromol.*, 2024, **273**, 133015.

29 H. M. Nassef, G. A. A. M. Al-Hazmi, A. A. Alayyafi, M. G. El-Desouky and A. A. El-Bindary, Synthesis and characterization of new composite sponge combining of metal-organic framework and chitosan for the elimination of Pb(II), Cu(II) and Cd(II) ions from aqueous solutions: Batch adsorption and optimization using Box-Behnken design, *J. Mol. Liq.*, 2024, **394**, 123741.

30 G. A. A. M. Al-Hazmi, A. A. Alayyafi, M. G. El-Desouky and A. A. El-Bindary, Chitosan-nano CuO composite for removal of mercury (II): Box-Behnken design optimization and adsorption mechanism, *Int. J. Biol. Macromol.*, 2024, **261**, 129769.

31 G. A. A. Al-Hazmi, A. A. El-Zahhar, M. G. El-Desouky, M. A. El-Bindary and A. A. El-Bindary, Efficiency of Fe3O4@ZIF-8 for the removal of Doxorubicin from aqueous solutions: equilibrium, kinetics and thermodynamic studies, *Environ. Technol.*, 2024, **45**, 731–750.

32 H. H. Alsharief, N. M. Alatawi, A. M. Al-bonayan, S. H. Alrefaee, F. A. Saad, M. G. El-Desouky and A. A. El-Bindary, Adsorption of Azorubine E122 dye via Na-mordenite with tryptophan composite: batch adsorption, Box–Behnken design optimisation and antibacterial activity, *Environ. Technol.*, 2023, **45**, 3496–3515.

33 S. H. Alrefaee, M. Aljohani, K. Alkhamis, F. Shaaban, M. G. El-Desouky, A. A. El-Bindary and M. A. El-Bindary, Adsorption and effective removal of organophosphorus pesticides from aqueous solution via novel metal-organic framework: Adsorption isotherms, kinetics, and optimization via Box-Behnken design, *J. Mol. Liq.*, 2023, **384**, 122206.

34 S. D. Al-Qahtani, M. Alhasani, N. Alkhathami, K. A. Abu Al-Ola, K. Alkhamis, M. G. El-Desouky and A. A. El-Bindary, Effective levofloxacin adsorption and removal from aqueous solution onto tea waste biochar; synthesis, characterization, adsorption studies, and optimization by Box–Behnken design and its antibacterial activity, *Environ. Technol.*, 2023, **45**, 4928–4950.

35 A. M. Alsuhaibani, M. S. Refat, A. M. A. Adam, M. G. El-Desouky and A. A. El-Bindary, Enhanced adsorption of ceftriaxone antibiotics from water by mesoporous copper oxide nanosphere, *Desalination Water Treat.*, 2023, **281**, 234–248.

36 A. K. Hajri, S. A. Alsherari, M. A. Albalawi, A. A. Alharbi, D. A. Albalawi and M. Q. Albalawi, Highly effective removal of cobalt from aqueous solution via reusable nanocomposite of metal organic frame work and activated algae encapsulated onto double layer biopolymer, *Inorg. Chem. Commun.*, 2025, **175**, 114162.

37 F. Alkhatib, S. F. Ibarhiam, A. A. Sari, N. M. Alatawi, N. D. Alkhathami, M. M. Aljohani and F. Shaaban, Effective hydrogen production from sodium borohydride using reusable cobalt based metal-organic framework supported polyurethane sponge, *J. Mol. Struct.*, 2025, **1331**, 141467.

38 N. Hassan, A. Shahat, A. El-Didamony, M. G. El-Desouky and A. A. El-Bindary, Equilibrium, Kinetic and Thermodynamic studies of adsorption of cationic dyes from aqueous solution using ZIF-8, *Moroc. J. Chem.*, 2020, **8**, 624–635.

39 G. H. Al-Hazmi, M. S. Refat, M. G. El-Desouky and A. A. El-Bindary, Effective adsorption and removal of industrial dye from aqueous solution using mesoporous zinc oxide nanoparticles via metal organic frame work: equilibrium, kinetics and thermodynamic studies, *Desalination Water Treat.*, 2022, **272**, 277–289.

40 A. S. Al-Wasidi, I. I. S. AlZahrani, A. M. Naglah, M. G. El-Desouky, M. A. Khalil, A. A. El-Bindary and M. A. El-Bindary, Effective Removal of Methylene Blue From Aqueous Solution Using Metal-Organic Framework; Modelling Analysis, Statistical Physics Treatment and DFT Calculations, *ChemistrySelect*, 2021, **6**, 11431–11447.

41 U. Saeed, R. Bousbih, A. Mahal, H. Majdi, N. Jahan, M. S. Jabir, M. S. Soliman, A. R. Ayub, N. H. Elsayed, S. Ali, R. A. Khera and M. Waqas, Engineering of asymmetric A1-D1-A2-D2-A1 type non-fullerene acceptors of 4T2CSi–4F derivatives to enhance photovoltaic properties: A DFT study, *J. Phys. Chem. Solids*, 2024, **192**, 112094.

42 N. H. Elsayed, N. A. Alamrani, R. A. S. Alatawi, M. Al-Anazi, D. A. K. Alenazi, A. S. Alhawiti, A. M. Almutairi, W. Al-Anazi and M. Monier, Ion-imprinted aminoguanidine-chitosan for selective recognition of lanthanum (III) from wastewater, *Int. J. Biol. Macromol.*, 2024, **270**, 132193.

43 N. Hassan, A. Shahat, A. El-Didamony, M. G. El-Desouky and A. A. El-Bindary, Mesoporous iron oxide nano spheres for capturing organic dyes from water sources, *J. Mol. Struct.*, 2020, **1217**, 128361.

44 G. H. Al-Hazmi, M. S. Refat, M. G. El-Desouky, F. K. M. Wali and A. A. El-Bindary, Effective removal of industrial dye from aqueous solution using mesoporous nickel oxide: a complete batch system evaluation, *Desalination Water Treat.*, 2022, **273**, 246–260.

45 H. S. AlSalem, M. Monier, R. A. S. Alatawi, A. A. H. Bukhari, M. A. Abdelaziz, A. K. Hajri and N. H. Elsayed, Enantio-separation of (±)-ibuprofen racemic mixture using functionalized molecularly imprinted resorcinol formaldehyde resin, *Polym. Int.*, 2023, **72**, 195–204.

46 H. S. AlSalem, F. A. Alotaibi, M. Monier, M. A. Abomuti, W. Miled, A. S. Alhawiti, A. A. H. Bukhari, R. A. S. Alatawi, N. H. Elsayed and I. Youssef, Enantio-selective molecularly imprinted β-resorcylic acid-modified resin for chiral separation of cathinone, *Mater. Chem. Phys.*, 2023, **305**, 127932.

47 T. M. Almutairi, H. H. Al-Rasheed, Z. M. Alaqil, A. K. Hajri and N. H. Elsayed, Green Synthesis of Magnetic Supramolecules β-Cyclodextrin/Iron Oxide Nanoparticles for Photocatalytic and Antibacterial Applications, *ACS Omega*, 2023, **8**, 32067–32077.

48 A. M. Alsuhaibani, M. S. Refat, A. A. Atta, M. G. El-Desouky and A. A. El-Bindary, Efficient adsorption and removal of tetracycline antibiotics from aqueous solutions onto nickel oxide nanoparticles via organometallic chelate, *Desalination Water Treat.*, 2022, **277**, 190–205.

49 D. Saha and S. Deng, Structural stability of metal organic framework MOF-177, *J. Phys. Chem. Lett.*, 2010, **1**, 73–78.

50 M. M. Aljohani, A. Abu-Rayyan, N. H. Elsayed, F. A. Alatawi, M. Al-Anazi, S. K. Mustafa, R. K. Albalawi and R. Abdelmonem, One-pot microwave synthesis of chitosan-stabilized silver nanoparticles entrapped polyethylene oxide nanofibers, with their intrinsic antibacterial and antioxidant potency for wound healing, *Int. J. Biol. Macromol.*, 2023, **235**, 123704.

51 A. S. Alhawiti, N. H. Elsayed, F. M. Almutairi, F. A. Alotaibi, M. Monier and G. J. E. Alatwi, Construction of a biocompatible alginate-based hydrogel cross-linked by Diels–Alder chemistry for controlled drug release, *React. Funct. Polym.*, 2023, **187**, 105578.

52 N. A. Alamrani, F. M. Almutairi, F. A. Alotaibi, D. A. K. Alenazi, M. Monier, D. A. Abdel-Latif and N. H. Elsayed, Developing thiosemicarbazide-modified/ion-imprinted chitosan for selective cadmium ion biosorption, *Mater. Today Chem.*, 2023, **30**.

53 B. Wang, J. Wang, R. Mao, Z. Li, Y. Cheng, Y. Niu and H. Chen, Synthesis of bifunctional silica aerogels for robust and simultaneous removal of Hg(II) and malachite green: Performance and mechanism, *Sep. Purif. Technol.*, 2025, **355**, 129773.

54 L. Lang, B. Wang, T. Liu, J. Wang, L. Zhu, Y. Liu and Y. Niu, Homogeneous synthesis of Schiff base modified PAMAM dendrimers/silica for efficient adsorption of Hg(II), *Chem. Eng. J.*, 2023, **477**, 147310.

55 B. Wang, L. Luan, Z. Li, J. Wang, Y. Liu, Y. Niu and H. Chen, Synthesis of heterostructured microspheres for efficient removal of malachite green and basic fuchsine, *Chem. Eng. Sci.*, 2025, **303**, 120956.

56 T. A. Altalhi, G. A. M. Mersal, M. H. H. Mahmoud, T. Kumeria, M. G. El-Desouky, A. A. El-Bindary and M. A. El-Bindary, Adsorption of doxorubicin hydrochloride onto thermally treated green adsorbent: Equilibrium, kinetic and thermodynamic studies, *J. Mol. Struct.*, 2022, **1263**, 133160.

57 A. A. El-Bindary, M. G. El-Desouky and M. A. M. El-Afify, Thermal and spectroscopic studies of some prepared metal complexes and investigation of their potential anticancer and antiviral drug activity against SARS-CoV-2 by molecular docking simulation, *Biointerface Res. Appl. Chem.*, 2022, **12**, 1053–1075.

58 I. Langmuir, The constitution and fundamental properties of solids and liquids. Part I. Solids, *J. Am. Chem. Soc.*, 1916, **38**, 2221–2295.

59 H. M. F. Freundlich, Over the adsorption in solution, *J. Phys. Chem.*, 1906, **57**, 385–471.

60 M. Dubinin, The equation of the characteristic curve of activated charcoal, *Proc. Acad. Sci. USSR, Phys. Chem. Sect.*, 1947, **55**, 327–329.

61 V. P. M. I. Tempkin, Kinetics of ammonia synthesis on promoted iron catalyst, *Acta Phys. Chem. USSR*, 1940, **12**, 327–356.

62 N. M. El-Metwaly, H. A. Katouah, M. G. El-Desouky, A. A. El-Bindary and M. A. El-Bindary, Fabricating of Fe_3O_4@Ag-MOF nanocomposite and evaluating its adsorption activity for removal of doxorubicin, *J. Environ. Sci. Health,*

Part A: Toxic/Hazard. Subst. Environ. Eng., 2022, **57**, 1099–1115.

63 M. G. El-Desouky, M. A. Khalil, A. A. El-Bindary and M. A. El-Bindary, Biological, biochemical and thermochemical techniques for biofuel production: An updated review, *Biointerface Res. Appl. Chem.*, 2022, **12**, 3034–3054.

64 M. G. El-Desouky, A. A. El-Bindary and M. A. El-Bindary, Low-temperature adsorption study of carbon dioxide on porous magnetite nanospheres iron oxide, *Biointerface Res. Appl. Chem.*, 2022, **12**, 6252–6268.

65 M. G. El-Desouky, M. A. G. Khalil, M. A. M. El-Afify, A. A. El-Bindary and M. A. El-Bindary, Effective methods for removing different types of dyes – modelling analysisstatistical physics treatment and DFT calculations: a review, *Desalination Water Treat.*, 2022, **280**, 89–127.

66 M. A. El-Bindary, M. G. El-Desouky and A. A. El-Bindary, Adsorption of industrial dye from aqueous solutions onto thermally treated green adsorbent: A complete batch system evaluation, *J. Mol. Liq.*, 2022, **346**, 117082.

67 S. K. Lagergren, About the theory of so-called adsorption of soluble substances, *Sven. Vetenskapsakademiens Handl.*, 1898, **24**, 1–39.

68 Y.-S. Ho and G. McKay, Sorption of dye from aqueous solution by peat, *Chem. Eng. J.*, 1998, **70**, 115–124.

69 W. J. Weber Jr and J. C. Morris, Kinetics of adsorption on carbon from solution, *J. Sanit. Eng. Div.*, 1963, **89**, 31–59.

70 M. H. Dehghani, A. Dehghan and A. Najafpoor, Removing Reactive Red 120 and 196 using chitosan/zeolite composite from aqueous solutions: Kinetics, isotherms, and process optimization, *J. Ind. Eng. Chem.*, 2017, **51**, 185–195.

71 G. H. Al-Hazmi, L. A. Albedair, A. M. Alsuhaibani, S. H. Alrefaee, I. Althagafi, Q. Mohsen, M. G. El-Desouky, A. A. El-Bindary and K. A. Asla, Synthesis and characterization of functionalized yttrium metal-organic frameworks encapsulated onto bi-polymers for effective removal of As(III); Adsorption isotherms, kinetic, and optimization via Box-Behnken design, *Mater. Today Commun.*, 2025, **45**, 112244.

72 W. A. El-Fattah, A. Guesmi, N. B. Hamadi, M. G. El-Desouky and A. A. El-Bindary, Smart nanocomposite of carbon quantum dots in double hydrogel (carboxymethyl cellulose/chitosan) for effectively adsorb and remove diquat herbicide: Characterization, thermodynamics, isotherms, kinetics, and optimizing through Box-Behnken Design, *Int. J. Biol. Macromol.*, 2025, **309**, 142806.

73 A. H. Jawad, N. N. Mohd Firdaus Hum, A. S. Abdulhameed and M. A. Mohd Ishak, Mesoporous activated carbon from grass waste via H3PO4-activation for methylene blue dye removal: modelling, optimisation, and mechanism study, *Int. J. Environ. Anal. Chem.*, 2022, **102**, 6061–6077.

74 A. H. Jawad, U. K. Sahu, M. S. Mastuli, Z. A. ALOthman and L. D. Wilson, Multivariable optimization with desirability function for carbon porosity and methylene blue adsorption by watermelon rind activated carbon prepared by microwave assisted H_3PO_4, *Biomass Convers. Biorefinery*, 2022, 1–15.

75 A. H. Jawad and S. Surip, Upgrading low rank coal into mesoporous activated carbon via microwave process for methylene blue dye adsorption: Box Behnken Design and mechanism study, *Diamond Relat. Mater.*, 2022, **127**, 109199.

76 W. Abd El-Fattah, A. Guesmi, N. B. Hamadi, A. Alzahrani, A. A. Alluhaybi and M. El-Desouky, Effective of mercury (II) removal from contaminated water using an innovative nanofiber membrane: Kinetics, isotherms, and optimization studies, *Int. J. Biol. Macromol.*, 2025, 143596.

77 M. M. Aljohani, S. D. Al-Qahtani, M. Alshareef, M. G. El-Desouky, A. A. El-Bindary, N. M. El-Metwaly and M. A. El-Bindary, Highly efficient adsorption and removal bio-staining dye from industrial wastewater onto mesoporous Ag-MOFs, *Process Saf. Environ. Prot.*, 2023, **172**, 395–407.

78 G. H. Al-Hazmi, A. M. A. Adam, M. G. El-Desouky, A. A. ElBindary, A. M. Alsuhaibani and M. S. Refat, Efficient Adsorption of Rhodamine B Using A Composite of Fe_3O_4@Zif-8: Synthesis, Characterization, Modeling Analysis, Statistical Physics and Mechanism of Interaction, *Bull. Chem. Soc. Ethiop.*, 2023, **37**, 211–229.

79 H. S. AlSalem, R. A. S. Alatawi, A. A. H. Bukhari, J. S. Alnawmasi, I. Zghab, M. G. El-Desouky, M. H. Almabadi, Z. H. Alnakhli and N. H. Elsayed, Adsorption and removal of Pb(II) via layer double hydroxide encapsulated with chitosan; synthesis, characterization adsorption isotherms, kinetics, thermodynamics, & optimization via Box-Behnken design, *Int. J. Biol. Macromol.*, 2024, **283**, 137517.

80 H. A. Siddiq, M. M. M. Madkhali, R. Ghubayra, A. N. M. A. Alaghaz, M. G. El-Desouky, M. A. El-Bindary and A. A. El-Bindary, Efficient removal of tetracycline by VCo-layered double hydroxide encapsulated with chitosan: Optimization via Box-Behnken design, and thermodynamics, *Int. J. Biol. Macromol.*, 2025, **296**, 139565.

81 A. Almahri, K. S. Abou-Melha, H. A. Katouah, A. M. Albonayan, F. A. Saad, M. G. El-Desouky and A. A. El-Bindary, Adsorption and removal of the harmful pesticide 2,4-dichlorophenylacetic acid from an aqueous environment via coffee waste biochar: Synthesis, characterization, adsorption study and optimization via Box-Behnken design, *J. Mol. Struct.*, 2023, **1293**, 136238.

82 A. A. Alluhaybi, A. Alharbi, K. F. Alshammari and M. G. El-Desouky, Efficient Adsorption and Removal of the Herbicide 2,4-Dichlorophenylacetic Acid from Aqueous Solutions Using MIL-88(Fe)-NH_2, *ACS Omega*, 2023, **8**, 40775–40784.

83 S. D. Al-Qahtani, M. Alhasani, N. Alkhathami, K. A. Abu Al-Ola, K. Alkhamis, M. G. El-Desouky and A. A. El-Bindary, Effective levofloxacin adsorption and removal from aqueous solution onto tea waste biochar; synthesis, characterization, adsorption studies, and optimization by Box–Behnken design and its antibacterial activity, *Environ. Technol.*, 2024, **45**, 4928–4950.

84 H. H. Alsharief, N. M. Alatawi, A. M. Al-bonayan, S. H. Alrefaee, F. A. Saad, M. G. El-Desouky and A. A. El-Bindary, Adsorption of Azorubine E122 dye via Na-mordenite with tryptophan composite: batch adsorption,

Box–Behnken design optimisation and antibacterial activity, *Environ. Technol.*, 2024, **45**, 3496–3515.

85 A. Almahri, M. Morad, M. M. Aljohani, N. M. Alatawi, F. A. Saad, H. M. Abumelha, M. G. El-Desouky and A. A. El-Bindary, Atrazine reclamation from an aqueous environment using a ruthenium-based metal-organic framework, *Process Saf. Environ. Prot.*, 2023, **177**, 52–68.

86 W. Fu and Z. Huang, Magnetic dithiocarbamate functionalized reduced graphene oxide for the removal of Cu(II), Cd(II), Pb(II), and Hg(II) ions from aqueous solution: Synthesis, adsorption, and regeneration, *Chemosphere*, 2018, **209**, 449–456.

87 M. Abd El-Wahab and M. G. El-Desouky, In silico antibacterial, anticancer, antioxidant, antidiabetic activity predictions of the dual organic peroxide 2,5-dimethyl-2,5-di(tert-butyl peroxyl)hexane, *Main Group Chem.*, 2024, **23**, 177–190.

88 M. Abd El-Wahab and M. G. El-Desouky, Impact of organic peroxide on a moderate molecular weight homo-polypropylene vis breaking, and mechanism of interaction, *Main Group Chem.*, 2024, **23**, 145–156.

89 N. Hassan, A. Z. El-Sonbati and M. G. El-Desouky, Synthesis, characterization, molecular docking and DNA binding studies of Cu(II), Ni(II), Zn(II) and Mn(II) complexes, *J. Mol. Liq.*, 2017, **242**, 293–307.

90 K. Chen, Z. Zhang, K. Xia, X. Zhou, Y. Guo and T. Huang, Facile synthesis of thiol-functionalized magnetic activated carbon and application for the removal of mercury (II) from aqueous solution, *ACS Omega*, 2019, **4**, 8568–8579.

91 Y. Shen, N. Jiang, S. Liu, C. Zheng, X. Wang, T. Huang, Y. Guo and R. Bai, Thiol functionalization of short channel SBA-15 through a safe, mild and facile method and application for the removal of mercury (II), *J. Environ. Chem. Eng.*, 2018, **6**, 5420–5433.

92 H. Shirzadi and A. Nezamzadeh-Ejhieh, An efficient modified zeolite for simultaneous removal of Pb(II) and Hg(II) from aqueous solution, *J. Mol. Liq.*, 2017, **230**, 221–229.

93 A. Saad, I. Bakas, J.-Y. Piquemal, S. Nowak, M. Abderrabba and M. M. Chehimi, Mesoporous silica/polyacrylamide composite: preparation by UV-graft photopolymerization, characterization and use as Hg(II) adsorbent, *Appl. Surf. Sci.*, 2016, **367**, 181–189.

94 Y. Fu, Y. Huang and J. Hu, Preparation of chitosan/MCM-41-PAA nanocomposites and the adsorption behaviour of Hg(II) ions, *R. Soc. Open Sci.*, 2018, **5**, 171927.

95 H. Wei, H. Wang, Y. Xia, D. Cui, Y. Shi, M. Dong, C. Liu, T. Ding, J. Zhang and Y. Ma, An overview of lead-free piezoelectric materials and devices, *J. Mater. Chem. C*, 2018, **6**, 12446–12467.

96 M. Shafiabadi, A. Dashti and H.-A. Tayebi, Removal of Hg (II) from aqueous solution using polypyrrole/SBA-15 nanocomposite: Experimental and modeling, *Synth. Met.*, 2016, **212**, 154–160.

97 B. Geng, Z. Xu, P. Liang, J. Zhang, P. Christie, H. Liu, S. Wu and X. Liu, Three-dimensional macroscopic aminosilylated nanocellulose aerogels as sustainable bio-adsorbents for the effective removal of heavy metal ions, *Int. J. Biol. Macromol.*, 2021, **190**, 170–177.

98 M. Naushad, T. Ahamad, G. Sharma, H. Ala'a, A. B. Albadarin, M. M. Alam, Z. A. ALOthman, S. M. Alshehri and A. A. Ghfar, Synthesis and characterization of a new starch/SnO2 nanocomposite for efficient adsorption of toxic Hg2+ metal ion, *Chem. Eng. J.*, 2016, **300**, 306–316.

99 G. A. A. Al-Hazmi, A. A. El-Zahhar, M. G. El-Desouky and A. El-Bindary, Superior adsorption and removal of doxorubicin from aqueous solution using activated carbon via thermally treated green adsorbent: isothermal, kinetic, and thermodynamic studies, *Environ. Technol.*, 2024, **45**, 1969–1988.

100 G. A. A. M. Al-Hazmi, A. A. Alayyafi, M. G. El-Desouky and A. A. El-Bindary, Guava seed activated carbon loaded calcium alginate aerogel for the adsorption of diclofenac sodium: Characterization, isotherm, kinetics, and optimization via Box-Behnken design, *Int. J. Biol. Macromol.*, 2024, **262**, 129995.

101 G. H. Al-Hazmi, L. A. Albedair, R. A. S. Alatawi, J. S. Alnawmasi, A. M. Alsuhaibani and M. G. El-Desouky, Enhancing trimethoprim pollutant removal from wastewater using magnetic metal-organic framework encapsulated with poly (itaconic acid)-grafted crosslinked chitosan composite sponge: Optimization through Box-Behnken design and thermodynamics of adsorption parameters, *Int. J. Biol. Macromol.*, 2024, **268**, 131947.

102 A. M. Alotaibi, J. S. Alnawmasi, N. A. H. Alshammari, M. A. Abomuti, N. H. Elsayed and M. G. El-Desouky, Industrial dye absorption and elimination from aqueous solutions through bio-composite construction of an organic framework encased in food-grade algae and alginate: Adsorption isotherm, kinetics, thermodynamics, and optimization by Box–Behnken design, *Int. J. Biol. Macromol.*, 2024, **274**, 133442.

103 A. M. Alsuhaibani, A. A. Alayyafi, L. A. Albedair, M. G. El-Desouky and A. A. El-Bindary, Efficient fabrication of a composite sponge for Cr(VI) removal via citric acid cross-linking of metal-organic framework and chitosan: Adsorption isotherm, kinetic studies, and optimization using Box-Behnken design, *Mater. Today Sustain.*, 2024, **26**, 100732.

104 W. A. El-Fattah, A. Guesmi, N. Ben Hamadi, M. G. El-Desouky and A. Shahat, A green synthesis of cellulose nanocrystals biosorbent for remediation of wastewater containing industrial dye, *Colloids Surf., A*, 2024, **681**, 132729.

105 A. Mohammed Alsuhaibani, A. A. Alayyafi, L. A. Albedair, M. G. El-Desouky and A. A. El-Bindary, Synthesis and characterization of metal–organic frameworks based on thorium for the effective removal of 2,4-dichlorophenylacetic pesticide from water: Batch adsorption and Box-Behnken Design optimization, and evaluation of reusability, *J. Mol. Liq.*, 2024, **398**, 124252.